# Physico-chemical parameters of Neoarchean syntectonic magmatism: the example of the Muscocho Pluton, Abitibi Subprovince

Lucie Mathieu[a,*], Baptiste Madon[a], Michael A. Hamilton[b]

[a] Centre d'études sur les ressources minérales (CERM), Département des Sciences appliquées, Université du Québec à Chicoutimi (UQAC), Chicoutimi, Québec, Canada

[b] Jack Satterly Geochronology Laboratory, Department of Earth Sciences, University of Toronto, Toronto, Ontario, Canada

*Corresponding author: L. Mathieu (lucie1.mathieu@uqac.ca; Tel: (+001)-418-545-5011 ext. 2538)

ORCID number (L. Mathieu): 0000-0001-8814-3118

Submitted as a regular paper to

Ore Geology Reviews

## Abstract

The Muscocho Pluton is one of a number of syntectonic Neoarchean granodiorite intrusions formed during the main deformation phase in the Abitibi Subprovince that lead to stabilization of the Superior craton. Such magma locally are associated with magmatic-hydrothermal styles of mineralization, interpreted by some works to reflect intrusion-related gold systems (IRGS). Determining whether magmas can transport enough Au to fertilize the upper crust during this tectonomagmatic interval requires insights into physico-chemical parameters such as pressure, temperature, and oxygen fugacity ($fO_2$). The $fO_2$ parameter is particularly important because it affects S-speciation and S-solubility, which correlates with Au-solubility in magmas. Retrieving such parameters from the metamorphosed, locally hydrothermally altered, and generally deformed Neoarchean rocks is particularly challenging. As such, this contribution uses fresh to altered granodiorites of the Muscocho Pluton, a 16 km diameter granodiorite intrusion spatially associated with polymetallic mineralization, to evaluate whether physico-chemical parameters can be retrieved from ancient altered rocks based on amphibole, apatite, and zircon chemistry. This study also has implications for the origins of the Muscocho Pluton, which ascended slowly toward the upper crust as a single pulse of evolved magma and became emplaced at about 12 km depth. The magma had an $fO_2$ above the Ni/NiO solid oxygen buffer (NNO +1), which is not considered optimal for Au transportation. The magma also formed a deep intrusion unable to provide magmatic fluids to trigger an efficient hydrothermal system. This study provides the basis for a systematic evaluation of the physico-chemical conditions within which syntectonic magmas evolved in the upper crust. Knowledge of these physico-chemical conditions are necessary to better constrain the IRGS metallogenic model.



**Keywords:** Muscocho Pluton; granodiorite; Abitibi Subprovince; syntectonic magmatism; physico-chemical parameters; intrusion-related gold systems (IRGS)

## 1. Introduction

The Abitibi Subprovince, Canada, is a Neoarchean greenstone belt renowned for its gold endowment. Gold mineralization is generally related to hydrothermal systems dominated by metamorphic fluids, referred to as orogenic gold deposits (Bateman et al., 2005; Gosselin and Dubé, 2005; Groves et al., 1998; Phillips and Powell, 2010). Other systems, however, display evidence of magmatic fluid influx and correspond to intrusion-related gold systems (IRGS) (Fayol and Jébrak, 2017; Ispolatov et al., 2008; Katz et al., 2017; Robert, 2001). The origin of fluids is debated in many mineralized zones as orogenic gold systems can be difficult to distinguish from IRGS.

Orogenic gold systems and IRGS can, however, be distinguished on the basis of field relationships (e.g., cross-cutting relationships between sulphides and intrusive rocks), mineralizing style (structurally-controlled quartz veins vs disseminated sulphide), and metallic assemblages, as IRGS tend to be characterised by polymetallic mineralization, whereas orogenic gold systems tend to be Au-only (Lang and Baker, 2001; Phillips and Powell, 2010; Robert, 2001). Nonetheless, orogenic gold systems and IRGS display similarities and are relatively contemporaneous (i.e., both form during the syntectonic period), which leads to debates over the classification of deposits, e.g., Canadian Malartic deposit, alternately interpreted as an IRGS (Helt, 2012) and as an orogenic gold system (De Souza et al., 2015).

The IRGS metallogenic model is also controversial because it remains undocumented as to whether Neoarchean magmas can transport Au, or whether magmatism played a minor role in fertilizing the upper crust during the late stage of the evolution of Neoarchean greenstone belts. Evaluating the amount of gold that syntectonic magmatism can and did transport requires the measurement of physico-chemical and chemical parameters such as oxidation state (or oxygen fugacity – $fO_2$) as well as the volatile and metal content of the magmas. This is because $fO_2$ affects S-speciation, thus influencing the amount of S that can be dissolved in magma; this, in turn, correlates with Au solubility (Botcharnikov et al., 2010). Physico-chemical parameters can only be estimated through a detailed characterization of individual intrusions.

Magmatism coeval with the late evolution of greenstone belts, including the Abitibi Subprovince, is known to be chemically diverse (Feng and Kerrich, 1992; Levesque et al., 1991; Sutcliffe et al., 1993), and up to nine magma types have been recently recognized (Moyen, 2019). Among these types, magmas either have crustal sources (e.g., tonalite-trondhjemite-granodiorite – TTG) or mantle sources metasomatized by TTG melts and fluids that produced sanukitoid and alkaline magmas, respectively (Moyen, 2019; Stern et al., 1989). Some petrogenetic models remain debated (Bédard, 1996), and the importance of source chemistry over magma hybridization and differentiation also remains uncertain (Mathieu et al., 2020a; Moyen, 2019).

In this context, identifying a favourable source from which Au-endowed magmas were extracted is not straightforward. This complexity limits the use of igneous petrology by exploration companies; for example, alkaline magmas are oxidized and may be most fertile (Cameron and Hattori, 1987; Jensen and Barton, 2000; Levesque, 1994; Rowins et al., 1991), although there are examples of Au mineralization related to non-alkaline systems (Fayol and Jébrak, 2017). Classification of magma types related (or not) to IRGS in the Abitibi Subprovince could help clarify the elements of the IRGS metallogenic model. Another approach, considered here, measures the physico-chemical parameters of intrusions to evaluate whether the magmas formed during the syntectonic period had the capacity to transport Au in the crust. Physico-chemical parameters are measured routinely from post-Archean systems (Miles et al., 2014; Ridolfi et al., 2010; Smythe and Brenan, 2016); however, these data are often not as easy to retrieve from the metamorphosed, locally hydrothermally altered, and generally deformed Neoarchean rocks and especially from the strongly altered magma intrusions related to IRGS. This study aims to evaluate the feasibility of such measurements and to evaluate the effect that hydrothermal alteration had on the minerals generally used to evaluate $fO_2$ and other physico-chemical parameters. To this end, fresh rocks (e.g., Sample MUS7) from the ca. 2.70 Ga Muscocho Pluton (Mortensen, 1993) are compared to moderately (Sample MUS3) and strongly (Sample MUS2) altered dykes. The Muscocho Pluton is a 16 km diameter granodiorite pluton located in the north-eastern corner of the Abitibi Subprovince (**Figure 1**), Chibougamau area, that may be related to polymetallic (IRGS?) mineralization (SIGEOM, 2020). This study evaluates the effect of hydrothermal alteration on apatite, amphibole and zircon

chemistry, through which we propose insights into the petrogenesis and mode of emplacement of the Muscocho Pluton. This study also provides a basis for a systematic measurement of the parameters of interest in Neoarchean intrusions (e.g., granodiorite, syenite); these measurements will help confirm or contradict the existing IRGS metallogenic model.

## 2. Geological setting

The thickest package of volcanic rocks in the Chibougamau area belongs to the ca. >2730 Ma to ~2716 Ma Roy Group, which sits on ca. 2790–2760 Ma volcanic units (Chrissie and Des Vents formations) and is overlain by the ca. <2704–2690 Ma sedimentary units of the Opémisca Group (**Figure 1**) (David et al., 2012; Leclerc et al., 2017, 2012). The Roy Group is divided into volcanic cycle 1 (Obatogamau and Waconichi formations), which consists of mafic to intermediate lava flows, and volcanic cycle 2 (Bruneau, Blondeau and Bordeleau formations), which consists of mafic flows topped by intermediate to felsic flows and fragmental units (Leclerc et al., 2017). In this contribution, the magmatic events that formed the Roy Group and its coeval plutons, as well as older volcanic rocks, will be referred to as the synvolcanic period, while later events that led to craton stabilization are considered to have occurred during the syntectonic period. Several deformation events are recognized to have affected the study area over this period. The main event is $D_2$, which is associated with N–S shortening related to terrane assembly, i.e., the oft-named Kenoran orogeny (Dallmeyer et al., 1975). The waning stage ($D_3$) of the main deformation event $D_2$ reactivated east-west-striking faults as transcurrent strike-slip faults (Daigneault and Allard, 1990).

Several intrusive bodies were emplaced during the synvolcanic period. These intrusions include layered tholeiitic complexes, such as the Lac Doré Complex (Allard, 1976; Mathieu, 2019), tonalite-trondjhemite-granodiorite (TTG) suites, such as the Eau Jaune Complex (Tait, 1992) and tonalite-trondjhemite-diorite (TTD) suites, such as the ca. 2714–2718 Ma (Krogh, 1982; Pilote et al., 1997)(Krogh, 1982; Pilote et al., 1997)(Krogh, 1982; Pilote et al., 1997)Chibougamau Pluton (Krogh, 1982; Mathieu and Racicot, 2019; Pilote et al., 1997) that is genetically related to Cu-Au porphyry–style mineralization (Pilote et al., 1997).

Syntectonic magmatism may be coeval with the sedimentary deposits of the Opémisca Group (**Figure 1**), including syn-sedimentary shoshonitic lava flows observed in the Haüy Formation (Piché, 1985). Other intrusive bodies, such as the granodioritic Chevrillon Pluton and the syenitic Saussure Pluton, intrude the Opémisca Group and likely formed late during the syntectonic period (**Figure 1**). Another category of intrusion is attributed to the syntectonic period based on U-Pb radiogenic dating. This includes tonalite and monzodiorite of the 2696 ± 3 Ma Barlow Pluton (Davis et al., 1995; Racicot et al., 1984), tonalite of the 2701–2705 Ma polyphase Chibougamau Pluton (David et al., 2011; McNicoll et al., 2008), tonalite-granodiorite of the 2697 ± 3 Ma Boisvert Pluton (Davis et al., 2005) and granodiorite-monzondiorite of the 2695 Ma Opémisca Pluton (Gariépy and Allègre, 1985).

Syntectonic magmatism is also represented by the 2701.2 +1.7/-1.3 Ma Muscocho Pluton (Mortensen, 1993). This 16 km diameter sub-circular pluton crosscuts volcanic rocks of the Obatogamau Formation (volcanic cycle 1; **Figure 1**). The Muscocho Pluton is homogeneous and composed of hornblende granodiorite with mafic enclaves observed locally along its margin (Daigneault, 1991; Racicot et al., 1984; Tait, 1992). A weak concentric magmatic foliation is defined by the preferred alignment of feldspar and amphibole. The Muscocho Pluton is surrounded by a 500–1000 m thick aureole of amphibolite facies volcanic rocks, while regional metamorphism is greenschist facies grade in most of the Abitibi Subprovince (Faure, 2015; Jolly, 1974). Within the aureole, contact metamorphism has obliterated the main foliation, i.e., $S_2$, associated with the regional $D_2$ event. This indicates that the Muscocho Pluton emplaced after or toward the end of the $D_2$ deformation event (Daigneault et al., 1990; Tait, 1992). Several dykes emanating from the pluton also cross-cut the $S_2$ foliation (Tait, 1992).

A number of polymetallic prospects are found along the northern margin of the Muscocho Pluton. The 'Lac Muscocho-Nord' Au prospect consists of disseminated pyrite and quartz veinlets observed in a granodiorite dyke intruded in basalt. The main alteration types are carbonatization and sericitization (SIGEOM, 2019a), and it is unclear whether the associated mineralization is related to an IRGS or to an orogenic gold system. The 'Lac Muscocho' prospect (Ni-Cu-PGE-Au-Ag-Zn) is hosted in mafic rocks of the Obatogamau Formation. It consists of stockwork, veinlets, as well as disseminated chalcopyrite,

pyrrhotite and pyrite. This prospect is associated with carbonatization, is spatially associated with a felsic dyke from the Muscocho Pluton and its metallogeny is unresolved (SIGEOM, 2019b). Other Au prospects are observed NE and SW of the pluton, including the volcanogenic 'Lac Merrill Sud-2' Au prospect and the 'Dominion Gulf' prospect (Au-Cu-Ag), both of which include quartz veins, carbonatization and disseminated sulphides. These prospects are likely orogenic gold systems formed during the syntectonic period (SIGEOM, 2020).

## 3. Methodology

### 3.1. Sampling and whole-rock analyses

Nine of the whole rock chemical analyses performed on rocks from the Muscocho Pluton were collected from the SIGEOM dataset (SIGEOM, 2020). We also included an additional five samples (standard thin sections) collected in 1983 (Daigneault, 1991) and since stored at UQAC. Additional sampling during the summers 2018 and 2019 targeted the Muscocho Pluton (Sample MUS7) and two dykes located next to the pluton (Samples MUS2 and MUS3). Sample MUS2 is a strongly sericitized and deformed (boudinage) 1-m-thick feldspar-phyric dyke located on the Dominion Gulf prospect (**Figure 1**). Sample MUS3 is a sericitized, feldspar- and quartz-phyric 0.5-m-thick irregular (deformed) dyke that crosscuts the mafic flows of the Obatogamau Formation (**Supplementary Material S1)**. Sample MUS7 is a representative, coarse-grained feldspar-hornblende-quartz–bearing granodiorite of the Muscocho Pluton.

Thick (50 μm) polished sections were obtained from these three samples (**Table S3A in Supplementary Material S2**). Petrographic observations were performed using an Olympus BX53M petrographic microscope equipped with a motorized stage and an SC50 camera. Image processing was performed using Stream 2.4 (Count&Measure extension, Olympus) and GIMP 2.10.14 software.

The nine whole-rock analyses compiled from the SIGEOM dataset were performed on behalf of the Ministère de l'Énergie et des Ressources Naturelles (MERN) in 1996 and 2013 (**Supplementary Material S3)**. Similar analyses were performed on Samples MUS2, MUS3, and MUS7 by ALS Chemex Ltd. Rigorous quality assurance – quality control (QA–QC) procedures were maintained, including the use of blanks, standards, and

duplicates, to obtain precise and accurate results. Major elements were analysed by inductively coupled plasma (ICP) atomic emission spectroscopy (AES) following acid digestion, applying a detection limit of 0.01 wt.%. Most trace elements were analysed by ICP mass spectrometry (MS) following lithium borate fusion, with detection limits ranging from 0.01 to 5 ppm (**Table S3B**).

### 3.2. Zircon separates

Zircon mineral concentrates were obtained from Samples MUS3 and MUS7. Sample MUS3 (5.43 kg) was initially processed at the Jack Satterly Geochronology Laboratory (JSGL) at the University of Toronto. The sample underwent conventional jaw crushing, followed by grinding using a Bico™ disk mill. Initial separation of heavy minerals was carried out by passing the ground sample and derived heavy concentrates multiple times over a shaking, riffled water table (Wilfley™). Further processing employed density separations with methylene iodide, and standard paramagnetic separations using a Frantz™ isodynamic separator. Final sample selection was achieved by handpicking in alcohol under a binocular microscope, choosing the freshest, least cracked, core- and inclusion-free grains of zircon for isotope dilution thermal ionization mass spectrometry (ID-TIMS, performed at University of Toronto). Representative best quality zircon grains from this concentrate were picked dry under a binocular microscope, transferred into an epoxy mount and polished to their mid-sections at UQAC.

A zircon separate for Sample MUS7 (2.03 kg) was obtained in the laboratories of Overburden Drilling Management Ltd. (ODM), Ottawa, Ontario. The rock was pulverized using the electric-pulse disaggregation method. The <1 mm fraction was processed by ODM using shaking tables and micro-panning to produce a zircon concentrate. Final zircon selection was achieved by dry handpicking under a binocular microscope, choosing the freshest and least cracked crystals, with selected grains prepared into epoxy mounts and polished at UQAC.

The morphology of the zircon grains embedded in epoxy was documented using backscattered electron (BSE) images produced using an FEI Inspect F50 scanning electron microscope (SEM) at Laval University. The BSE images revealed cracks, altered areas (rims of most zircons), and the location of apatite inclusions. Further characterization was

performed using a petrographic microscope (Olympus Instruments) and cathodoluminescence (CL8200 Mk5-1 Optical) at UQAC (**Supplementary Material S4)**.

### 3.3. Mineral chemistry analyses

Silicates and phosphate (amphibole, feldspar, phyllosilicate, and apatite) were analysed using a CAMECA SX-100 microprobe at Laval University, Quebec. Operating conditions for these analyses employed a beam current of 20 nA, an accelerating voltage of 15 keV and a beam size of 2 µm (apatite) and 5 µm (silicates). Analyses were calibrated using the 12 standards listed in Table S5A. These analyses provided an assessment of constituent elements of each mineral, including internal standards for the laser ablation analyses, as well as their volatile content (Cl, F, S). Full analytical results are provided as **Supplementary Material S5**.

Quantitative laser ablation ICP-MS (LA-ICP-MS) analyses of apatite, zircon (trace element analyses), amphibole, feldspar, titanite and quartz were carried out at the LabMaTer laboratory (UQAC) on Samples MUS2, MUS3, and MUS7 (thin sections and epoxy mounts; **Supplementary Material S6**). These in situ analyses were run using a RESOlution ArF-193nm excimer laser ablation system (Australian Scientific Instrument) equipped with a double-volume cell S-155 (Laurin Technics) coupled to an Agilent 7900 ICP-MS. The parameters used for these analyses were a beam size of 19 to 33 µm, a laser frequency of 15 Hz, a dwell time of 5 to 20 ms for each element and an energy density of 5 J/cm$^2$ (**Table S6A**). Silicates, apatite, and reference materials were analysed using spots (acquisition time = 30 s) and lines (stage speed = 5 µm/s) after measuring the gas blank for 20 s.

For most elements, calibration was performed using the USGS reference material GSE-1g, which is a fused-basaltic glass doped with ~500 ppm of each trace element (Jochum et al., 2005b). For S, calibration relied on the NIST610 reference material, which is a glass doped with ~500 ppm of each trace element (Jochum et al., 2011). Data quality was monitored using the NIST610, NIST612, 91500-zircon, Durango apatite and GSD reference materials (Jochum et al., 2005a). The results are in good agreement with working values, except for P (all the standards), as well as K and Fe (NIST standards; **Tables S6A–S6G**). The

Durango standard also provided poor results, possibly due to heterogeneities in the analysed portions of this apatite standard (**Table S6F**).

Trace elements determined using laser ablation (LA-ICP-MS) methods at UQAC were reduced using LADR 1.1.01 software (http://norris.org.au/ladr). The internal standards $^{29}Si$ (zircon, quartz), $^{27}Al$ (feldspar), $^{42}Ca$ (apatite, amphibole), and $^{49}Ti$ (titanite) were used. For amphibole, plagioclase, and orthoclase, the respective values for Ca (11.3 wt.%), Al (18.7 wt.%), and Al (22.0 wt.%) were deduced from microprobe analyses. For the other minerals, stoichiometric values of 16.12 wt.% Si (zircon), 46.74 wt.% Si (quartz), 39.00 wt.% Ca (apatite) and 18.16 wt.% Ti (titanite) were used (Webmineral mineralogy database http://webmineral.com).

### 3.4. Geochronology analyses

In situ U-Pb isotopic ratios were measured using the laser ablation (LA-ICP-MS) analytical methods described in the previous section. These analyses were performed on zircons embedded in epoxy (Samples MUS3 and MUS7) (**Supplementary Material S7**). Calibration was performed using the Plesovice and 91500-zircon reference materials (Sláma et al., 2008; Wiedenbeck et al., 2004). Data quality was monitored using an in-house zircon reference material from the Sept-Iles intrusion (Higgins and van Breemen, 1998). Results agree well with certified values (**Tables S7A–S7C**). The exception was the results from some zircons analysed on the first day; most of these analyses were discarded (**Table S7E**).

Best quality zircon from Sample MUS3 separated in Toronto were pre-treated for conventional isotope dilution mass spectrometry (ID-TIMS) using a modified chemical abrasion method (Mattinson, 2005). Zircon grains were annealed in quartz crucibles at 900 °C for approximately 48h, and subsequently etched in concentrated hydrofluoric (HF) acid for up to several hours in Teflon vessels at 200°C.

Weights of mineral fractions chosen for ID-TIMS analyses were estimated from scaled digital photomicrographs using the density of zircon. Samples were given a brief ultrasonic treatment and washed before dissolution. A mixed $^{205}Pb$-$^{235}U$ isotopic spike was added to the dissolution capsules during sample loading. Zircon grains were dissolved using concentrated HF in Teflon bombs at 200 °C for 3–4 days, then dried and re-dissolved in

3N HCl overnight (Krogh, 1973). Uranium and Pb were isolated in 50-µL anion exchange columns using HCl elutions, dried down, and then loaded onto outgassed rhenium filaments with silica gel (Gerstenberger and Haase, 1997). Lead and $UO_2$ were analysed on a VG354 mass spectrometer using a Daly collector in pulse counting mode. The mass discrimination correction for this detector was constant at 0.07%/AMU. Dead time of the Daly system was 16 ns for Pb during the analytical period, monitored using the SRM982 Pb standard.

The isotopic ratio determined using laser ablation (LA-ICP-MS) analyses performed on zircon (Samples MUS3 and MUS7) at UQAC were reduced using the IOLITE software (Paton et al., 2011). Data were then displayed on the Concordia diagram using the online IsoplotR software (Vermeesch, 2018), and 73 discordant analyses (out of $n$ = 93) were identified (**Table S7E**). The 20 remaining analyses are concordant ages with an uncertainty of 10 Ma (standard deviation) and were plotted on the weighted mean diagram using the IsoplotR software.

Mass spectrometer (ID-TIMS) data were reduced using in-house software (UtilAge program) coded by D. Davis (JSGL, University of Toronto). All common Pb was assigned to procedural blank. Initial Pb from geological sources above 1 pg was corrected using a Pb-evolution model (Stacey and Kramers, 1975). Plotting of Concordia curves and averaging of age results were carried out using the Isoplot 3.71 add-in for MS Excel (Ludwig, 2009). Uncertainties in the U-decay constants, though shown on the Concordia diagram, were not factored into the calculated weighted average age (**Supplementary Material S8**).

## 4. Results

In this section, data are presented using the following notation: $a \pm b$, with $a$ the median and $b$ the standard deviation.

### 4.1. Whole-rock geochemistry

The studied rocks ($n$ = 12) display a narrow range of chemical variation and are located at the edge of the granodiorite field (**Figure 2a**) on a total alkalis vs silica (TAS) diagram (Le Bas et al., 1992). Fractional crystallization is indicated by an increase of the Si content

from 64 to 70 wt.% $SiO_2$, which is accompanied by a Ca decrease and alkali increase (**Figure 2b**). Also, K increases slightly faster than Na during differentiation, as is commonly observed in modern calc-alkaline magmas.

The Muscocho Pluton and nearby dykes are metaluminous and have calc-alkaline affinities according to the AFM (Barker, 1978) and Th/Yb vs Zr/Y (Ross and Bédard, 2009) diagrams (**Table S3D**). The studied samples plot outside the general field of Archean TTG compositions on a Na-K-Ca diagram (**Figure 2b**). The $Fe_2O_3/Fe_2O_{3T}$ ratio is 0.50 ± 0.04 ($n$ = 8 samples from the pluton), which falls within the range to slightly higher than the iron ratio of 0.4-0.5 compiled for rocks with similar silica and alkali contents (Middlemost, 1989).

The studied samples display fractionated trace element patterns on multielement diagrams (**Figure 3a, b**). They contain more HREE than most TTG suites (Moyen and Martin, 2012) and display moderate LREE, LILE, and HFSE enrichments. The dykes are distinctly less LREE-rich than the pluton (**Figure 3b**). The total REE content of the Muscocho Pluton decreases with increasing $SiO_2$ content, and no Eu anomaly is observed. The Muscocho Pluton displays Ta-Nb-Ti negative anomalies, and the Ta-Ti negative anomalies are less pronounced in the dykes. The rocks of the pluton also display negative Zr-Hf anomalies, while these anomalies are positive in the dykes.

Zircon-saturation temperature is estimated using major element and Zr contents (Watson and Harrison, 1983). A temperature of 1012 ± 5 °C is obtained ($n$ = 12; **Table S3B**). This indicates that if the magma was free of inherited zircons, then zircon may have started crystallizing at around 1012 °C.

### 4.2. Petrology

The Muscocho Pluton granodiorite mostly contains feldspar (plagioclase ± alkali feldspar), quartz, epidote, and green hornblende, as well as some biotite. The accessory phases include titanite, apatite, magnetite, and zircon. Petrographic observations and image processing (**Figure 4a, d**) reveal that Sample MUS7 contains approximately 14 vol.% amphibole, 15 vol.% quartz, 50 vol.% plagioclase, 20 vol.% alkali feldspar, and 1–2 vol.% of accessory phases (**Table S3C**). Other samples from the pluton also contain biotite that is locally chloritized.

Sample MUS7 (granodiorite) and other samples from the Muscocho Pluton have porphyritic textures, containing euhedral plagioclase and amphibole that are 0.5 to 2.5-mm-long (up to 5 mm) and 0.5 to 1.5-mm-long, respectively. Plagioclase and amphibole crystallized early and are embedded in a matrix of quartz and alkali feldspar (**Figure 4a**). Amphibole is euhedral, displays oscillatory zoning (**Figure 4e and supplementary material S2**) and is slightly altered (chloritised cracks mostly). Plagioclase grains are replaced by white mica and epidote, but maintain their magmatic texture; i.e., euhedral forms and oscillatory zoning. Large (~0.1 mm in diameter) euhedral epidote are observed as inclusion in amphibole (**Figure 4d**) and biotite (**supplementary material S2**). Quartz is generally xenomorphic, 0.3 to 0.7-mm-long, and has been deformed, as indicated by undulatory extinction and the onset of subgrain formation. Some of the quartz corresponds to smaller, rounded grains (~0.5 mm in diameter), rimmed by small (<50 μm) alkali feldspar and embedded in xenomorphic quartz (**Figure 5a**). The other alkali feldspars are 0.1 to 0.5-mm-long euhedral grains. Biotite occurs replacing hornblende, or as a xenomorphic interstitial mineral. Apatite (10 to 100-μm-long) and the few zircon grains observed in thin section are mostly found as inclusions in amphibole and rarely in feldspar, while euhedral titanite (10 to 500-μm-long) and rounded magnetite (≥100 μm) are mostly found in quartz at the edge and outside of amphibole (**Figure 4a**). Apatite is elongated with hexagonal basal section and displays oscillatory zoning.

The dykes are also granodioritic in composition (**Figure 2c**) and display a similar mineral assemblage to the Muscocho Pluton. In Sample MUS3, quartz phenocrysts (0.5-mm-long) are rounded and deformed (subgrains observed), whereas the plagioclase phenocrysts (1 to 2-mm-long) are euhedral and altered (sericitized and epidotized). Alkali feldspar phenocrysts are present as clusters of 0.1-mm-long crystals, the ferromagnesian silicate minerals are clusters of amphibole, biotite, and chlorite, and the matrix is a fine-grained assemblage of quartz and feldspar (**Figure 4b**). The MUS2 dyke is more strongly altered, wherein the amphibole has been entirely replaced by chlorite, and the feldspar phenocrysts (1 to 2-mm-long) and those in the finer matrix are replaced by clusters of white mica, carbonate, epidote, and quartz (**Figure 4c**). In Samples MUS3 and MUS2, apatite is elongated and small (1 to 10-μm-long) or rounded and large (up to 300-μm-long), and

phyllosilicate alignment defines foliation planes. In contrast, deformation fabrics in the Muscocho Pluton samples are limited to absent.

Zircon in Samples MUS7 and MUS3 was studied in additional detail via hand-picked separates embedded in polished epoxy mounts. The majority of grains are prismatic, have altered outer rims, and some display internal alteration along fractures (**Figure 5b**). Zircons from Sample MUS3 are occasionally more altered than those of Sample MUS7, particularly in higher U (metamict) domains. Thinly spaced and regular oscillatory zoning characterizes the zircon of both samples, and the main included phase is apatite. For Samples MUS3 and MUS7, the zircon are 93 ± 32-µm and 96 ± 35-µm-long, respectively, and have aspect ratios of 1.79 ± 0.60 and 1.90 ± 0.46.

A simplified normative calculation is applied to whole-rock analyses to estimate the proportions of the main phases. For this calculation, stoichiometric composition (quartz, apatite, feldspar, magnetite, titanite) and median structural formulas deduced from microprobe analyses performed on amphibole from Sample MUS7 (6.72 Si, 1.35 Al, 4.57 Mg + $Fe^{2+}$, 1.75 Ca, 0.48 Na, 0.12 K) were used. A $Fe_2O_3/Fe_2O_{3T}$ ratio of 0.50 was used to estimate FeO and $Fe_2O_3$ for the rocks when these values were unavailable. Excess water is considered throughout the calculation. Apatite, titanite, amphibole, magnetite, and feldspar were calculated successively to exhaust P, Ti, Fe+Mg, $Fe^{3+}$, and Na-Ca-K. Normative quartz is calculated using the remaining amount of Si.

The calculated normative compositions are considered in the quartz-alkali feldspar-plagioclase (Q-A-P) ternary space (Le Maitre et al., 2002; Streckeisen, 1979). Petrographic observations suggest that the alkali feldspar contains a limited amount of perthite and is likely orthoclase. The normative minerals are thus plotted on the Q-A-P ternary diagram assuming that P = (anorthite + albite) and A = orthoclase. The analysed rocks cluster tightly, fall mostly in the field of granodiorite (**Figure 2c**) and follow the differentiation trend of intermediate-K calc-alkaline magmas (Lameyre and Bowden, 1982). Normative mineral proportions are also plotted in the quartz-albite-orthoclase ternary for haplogranite (Johannes and Holtz, 1996), after correcting for anorthite (Blundy and Cashman, 2001); the studied rocks lie close to the 10 kbar quartz-feldspar cotectic (**Figure 2d**).

### 4.3. Mineral chemistry

Constituent elements for the minerals of interest were determined using microprobe analyses. In pluton Sample MUS7, feldspar ($n$ = 14 microprobe analyses) are either oligoclase ($An_{11-14}$) or orthoclase ($Or_{95-98}$) (**Figure 6a**). In dyke Sample MUS3 ($n$ = 14), feldspar are also oligoclase ($An_{10-18}$) or orthoclase ($Or_{97}$), while those of dyke Sample MUS2 are too altered to be classified. The structural formula of amphibole is calculated using several methods (Hawthorne et al., 2012; Leake et al., 1997; Ridolfi et al., 2010), all of which provide similar results. Samples MUS3 and MUS7 contain mostly hornblende, as well as hastingsite for Sample MUS3 only. The Mg# (MgO/[FeO+MgO]) of amphibole is 0.32 ± 0.02 (MUS3) and 0.48 ± 0.02 (MUS7).

Apatite compositions are fluoroapatite having trace amounts of Cl and OH. The apatite of Sample MUS3 contains more Cl than that of MUS7 (**Figure 6b**). The apatite of MUS2 and MUS3 are also S-rich, while the S content has a bimodal distribution in the apatite of Sample MUS7 (**Figure 6b**). The most S-rich apatite are also highest in Na and, in part, Fe (**Figure 6c, d**). Altered apatite can be identified on the basis of their Fe, Mn, and Ca contents (Dorais et al., 1997; Piccoli and Candela, 2002), indicating the presence of both pristine magmatic apatite (S-, Na-, and Fe-poor) and altered apatite (S-, Na-, and Fe-rich) in the studied rocks (**Figure 6c, d**).

The REE content of the studied minerals was investigated using LA-ICP-MS analyses. Feldspar contains a limited amount of REE, with most analyses having concentrations close to the detection limit. In addition, most feldspars are sericitized, and alteration may have modified the REE patterns. Nonetheless, Sample MUS7 contains the largest amount of unaltered feldspar, and these display LREE-enrichments and pronounced positive Eu anomalies (**Figure 7a**). Amphiboles from the same sample display typical REE profiles with LREE-enrichment and Eu-negative anomalies (**Figure 7b**). The amphiboles of Sample MUS3 are LREE-depleted.

Apatite displays a similar pattern, with those in Sample MUS7 containing more LREE than the apatite from the other samples (**Figure 7c**). Apatite exhibits a negative Eu anomaly in the bulk of samples, probably because the melt became Eu-depleted (because of plagioclase fractionation) before becoming apatite-saturated. Alteration also affected the apatite of Sample MUS7 and decreased the La and Ce content of about half of the analysed apatites.

The La-poorest zircon display typical REE patterns, with LREE-depletion, positive Ce anomalies, and slightly negative Eu anomalies (**Figure 7d**). The REE profiles of relatively La-enriched zircon (Sample MUS3 mainly) is less typical and points to alteration and the likely presence of apatite micro-inclusions.

### 4.4. Geochronology

Three zircon fractions, comprising between 1-2 grains each, were selected from Sample MUS3 for ID-TIMS analysis at the JSGL facility. Isotopic data for these fractions are negligibly discordant (0.4-0.7%) and yield a narrow range of model $^{207}Pb/^{206}Pb$ ages from 2699.7 to 2701.3 Ma. A weighted mean $^{207}Pb/^{206}Pb$ age for these three analyses is 2700.2 ± 1.6 Ma (2σ, MSWD = 0.21; **Figure 9**), which we interpret as reflecting the magmatic crystallization age for this granodiorite dyke emplaced immediately east of the Muscocho Pluton. The emplacement age for this dyke is identical, within error, of that established for the Muscocho Pluton, dated at 2701.2 +1.7/-1.3 Ma (Mortensen, 1993).

The uniform nature of the zircon age population in dyke MUS3 confirms a near-certain magmatic connection to the immediately adjacent Muscocho Pluton. However, the earlier ID-TIMS study, on both single and multigrain fractions from the Muscocho Pluton itself, revealed a significant proportion (60%) of older, inherited zircons with minimum ages of ca. 2705 Ma and ca. 2738 Ma (Mortensen, 1993). Therefore, we considered it essential to demonstrate that zircon grains from Sample MUS7 faithfully represented the established magmatic age (ca. 2701 Ma) population, and these zircons were analysed for U-Pb using the LA-ICP-MS at the LabMaTer facility (UQAC) in order to screen out inherited zircon. Although a majority of spot measurements were rejected due to discordance, the results for 9 of 11 most concordant analyses from MUS7 yield a weighted average $^{207}Pb/^{206}Pb$ age of 2701 ± 5 Ma (MSWD = 1.4; **Figure 10 and Supplementary material S7**), in excellent agreement with estimated igneous age (Mortensen, 1993). The LA-ICP-MS technique was also used to further characterize the zircons of Sample MUS3. Only 9 of 28 analyses provided concordant ages and yield a weighted average $^{207}Pb/^{206}Pb$ age of 2719 ± 5 Ma (*n* = 7 of 9 analyses; **Supplementary material S7**).

### 4.5. Physico-chemical parameters

Prior to calculating the physico-chemical parameters using apatite, amphibole, and zircon chemistry (**Figure 8**), the activity of Si ($a_{SiO_2}$) and Ti ($a_{TiO_2}$) is estimated. The studied rocks contain quartz that likely co-crystallized with the studied minerals (**Figure 4a**), and the $a_{SiO_2}$ parameter can be assumed to be equal to 1. The main Ti-bearing mineral is titanite in the studied rocks. The activity of Ti is estimated by assuming that whole-rock analyses are representative of melt composition (the validity of this approximation will be discussed later), which provides a median value of 2.73 for the FM parameter (Hayden and Watson, 2007). Using a temperature of 850 °C, the $a_{TiO_2}$ parameter is estimated to be 0.73 (MUS2), 0.64 (MUS3) and 0.58 (MUS7). These values are reasonable as a typical $a_{TiO_2}$ value is 0.6 or more in silicic melts at typical magmatic temperatures (Hayden and Watson, 2007).

Using amphibole chemistry, physico-chemical parameters were calculated using the AMP-TB.xls spreadsheet (Ridolfi et al., 2010). The basis for this method is a compilation of amphibole chemistry from calc-alkaline magmas produced in subduction-related systems. It includes empirical thermobarometric formulations based on independent compositional components of a single phase, i.e., amphibole (Ridolfi et al., 2010). The calculated parameters are available as supplementary material to this contribution (**Tables S5G and S6L**). They are summarized in **Table 1** and indicate that amphibole crystallized in the upper crust (**Figure 8a**) under moderate (MUS3) to slightly elevated (MUS7) $fO_2$ conditions (**Figure 8b**). The water content was elevated at the time of amphibole crystallization (~ 5 wt.% $H_2O$; **Figure 8c**), whereas the sampled rocks only contain ~ 1 wt.% $H_2O$ (**Table S3B**).

Pressure was also estimated using an Al-in-hornblende barometer (Mutch et al., 2016) that applies to shallow granitic intrusions with the mineral assemblage observed in the Muscocho Pluton, i.e., amphibole + plagioclase + biotite + quartz + alkali feldspar + titanite + magnetite + apatite. Using bulk amphibole compositions, this method provides pressure estimates that are twice those obtained using the Ridolfi et al. (2010) barometer (**Table 1**). No significantly different results are obtained when considering the core or rim of amphibole; as an example, for the L7_L2 analysis, pressures of 3.46 and 3.24 kbar are obtained when considering the core and rim, respectively, of an amphibole in contact with oligoclase (**Table S6L**).

Oxidation fugacity was estimated using the Mn-content of apatite (Miles et al., 2014). This method provides a log($fO_2$) value of -11 for Samples MUS2, MUS3, and MUS7 ($n$ = 34; **Table S6I**). Assuming a pressure of 2 kbar (**Figure 8a**), this corresponds to $fO_2$ conditions close to the Ni/NiO solid oxygen buffer (NNO), of NNO +1 (at 900 °C) or NNO (at 950 °C). Using another method (Azadbakht et al., 2018), $fO_2$ was estimated using the amplitude of the Eu anomaly observed in apatite (**Figure 8d**). This points to oxidizing conditions for most apatite, except for half of the apatite of Sample MUS7 that may have crystallized under moderately oxidizing conditions (**Figure 8d**).

Temperature was also appraised using the Ti-in-zircon thermometer (Ferry and Watson, 2007), which provides a narrow range of temperatures for zircons containing <0.1 ppm La (**Figure 8e**). These temperatures are approximately 720 °C for Samples MUS3 and MUS7 ($n$ = 69; **Table 1**). Oxidation state was then calculated (Smythe and Brenan, 2016) using the $a_{SiO_2}$ and $a_{TiO_2}$ parameters discussed earlier, a melt composition assumed to be represented by whole-rock analysis except for water content that is estimated using amphibole chemistry (see above). This parameter is 6.2 wt.% $H_2O$ and 4.6 wt.% $H_2O$ for Samples MUS3 and MUS7, respectively (**Figure 8f**). For zircon containing <0.1 ppm La, the oxidation state is estimated to be higher in MUS3 than in MUS7 (**Figure 8f**, **Table 1**).

Temperature was also calculated using Ti-in-quartz chemistry. The studied quartz is enriched in mineral and fluid micro-inclusions, and the calculation was only performed on the inclusion-poorest quartz with a sum of trace elements <0.05 wt.%. Using the TitaniQ method (Wark and Watson, 2006) and the $a_{TiO_2}$ parameter discussed previously, the calculated temperature is about 630 °C ($n$ = 9; **Tables 1 and S6H**).

## 5. Discussion

### 5.1. Field relationships and age

The Muscocho Pluton is a small-volume plug located in the NE corner of the Abitibi Subprovince. It is relatively undeformed and intersects foliated volcanic rocks. Based on these field relationships and on U-Pb dating, the pluton formed late, at ca. 2.70 Ga, after or toward the end of the main deformation phase ($D_2$) that affected the Chibougamau area, as previously interpreted (Daigneault et al., 1990; Tait, 1992). The studied dykes (Samples MUS2 and MUS3) likely emanated from the Muscocho Pluton based on U-Pb dating and

chemistry (see next section). These dykes are foliated, indicating that the Muscocho Pluton was likely emplaced before the end of the $D_2$ phase or between the $D_2$ and $D_3$ deformation events, toward the end of the syntectonic period.

The pluton may be genetically related to polymetallic mineralization (IRGS?), even if dedicated studies are required to determine the origin of the Lac Muscocho and Lac Muscocho-Nord mineralization (**Figure 1**). The polymetallic nature of these prospects and their spatial association with syntectonic dykes, however, are criteria generally used to identify IRGS-style of mineralization (Robert, 2001). In the Abitibi Subprovince and other greenstone belts, IRGS have been related to so-called 'syenite' and/or 'granodiorite' magmatism (Levesque et al., 1991; Robert, 2001; Rowins et al., 1991). The Muscocho Pluton is a good example of the latter type of magma. A standing question is whether such magmas have the capacity to transport Au to the upper crust. In the following sections, the Muscocho magma is characterized and critical parameters for Au transportation, i.e., $fO_2$ and other physico-chemical factors (temperature, pressure, and water content), are discussed in detail.

### 5.2. Magma type

The Muscocho Pluton and related dykes are granodiorites with homogeneous chemistries. They correspond to a differentiated magma that was likely emplaced in the upper crust by a single intrusive event. The major element content (Fe, Mg, alkali) and the evolution of the K/Na ratio are consistent with a calc-alkaline affinity (**Figure 2a, b, c**). Textures are consistent with the fractionation of epidote, oligoclase, hornblende, and ± quartz (large euhedral minerals) that lead to Si- and K-enrichment and to the late fractionation of interstitial quartz, orthoclase, and, in parts of the pluton, biotite.

The total REE content of the magma decreases with increasing $SiO_2$ content (**Figure 3**), which points to a fractionation controlled by amphibole and, possibly, apatite. The dykes (Samples MUS2 and MUS3) show lower overall REE content than the Muscocho Pluton, which may point toward a more pronounced differentiation. However, this is possibly more likely due to alteration as the dykes are more altered than the pluton, and LREE are mobile in many hydrothermal systems (Williams-Jones et al., 2012). Hydrothermal alteration may also explain why the dykes plot off-trend on the Q-A-P ternary diagram (**Figure 2c**).

Despite alteration, the dykes and pluton are granodiorites that display similar mineral assemblages, ages, and chemistry, and are likely to be co-magmatic. The main chemical differences are the Zr-Hf anomalies and the amplitude of the Ta-Ti anomalies, possibly because accessory phases (zircon and titanite) had started crystallizing when the dykes formed, and these phases were distributed unevenly between the dykes and the main pluton.

The magma that formed the studied intrusions had a ferrous and ferric iron content within the range of that of magmas having similar Si contents (Middlemost, 1989). This magma also crystallized magnetite, which points to a moderate to elevated $fO_2$. Negligible Eu anomalies are observed in the whole rock REE profiles. This could also indicate a moderate to elevated $fO_2$, but bulk Eu anomaly (whole rock analyses) is hard to interpret as it is influenced by the fractionation and accumulation of feldspar and amphibole, which preferentially incorporate $Eu^{2+}$ and $Eu^{3+}$, respectively (Drake and Weill, 1975; Klein et al., 1997). The Eu anomaly observed in these minerals rather suggests moderate $fO_2$ (**Figure 7**).

In the light of these chemical data, the Muscocho magma is characterized using the recently published classification of Moyen (Moyen, 2019). The studied pluton is neither a TTG (HREE and K contents are too high), a biotite granite, or other peraluminous anatectic melt—Al-content is too low for a sedimentary source, and a tonalitic source would not produce K-bearing magma—nor an alkaline intrusion, as LREE and K-Na contents are too low. It may thus belong to one of the mantle-derived magma types, i.e., the sanukitoid or HKCA (high-K calc-alkaline granitoid) types (Moyen, 2019). The studied intrusions are felsic rocks, and in the absence of mafic members, a mantle source cannot be ascertained. Also, sanukitoids are defined as magmas enriched in compatible and incompatible elements (Stern et al., 1989); however, as they differentiate, these defining characteristics are obliterated. The HKCA group, in turn, has no clear chemical definition (Moyen, 2019). The Muscocho Pluton is a K-bearing intrusion moderately enriched in LREE and LILE, and it likely has an enriched source. By elimination (see above), this source may be an enriched mantle (metasomatized?). The magma is also water-rich, as indicated by amphibole fractionation, and its $fO_2$ is moderate to elevated. Mantle sources may contain Au and may be essential to produce Au-rich magmas, and efforts should be pursued to evaluate the Au and base metal content of the Neoarchean mantle (Lawley et al., 2018).

### 5.3. Hydrothermal alteration

As discussed in the previous section, bulk rock chemistry has been slightly modified by hydrothermal alteration, which mostly affected the Na-K contents (**Figure 2a, b**) and induced losses of LREE elements (**Figure 3**). Alteration-induced losses of LREE are also observed in amphibole (MUS3) and apatite (Samples MUS2, MUS3, and half of the MUS7 apatite). For zircon, secondary processes increased its LREE content.

Alteration also induced increases in the S, Na, and Fe content of apatite (**Figure 6**). This increase correlates with textural changes observed in cathodoluminescence images that show growth zoning (magmatic apatite) as well as spongy and homogeneous texture (hydrothermally altered apatite). In zircon, elevated La content is a good proxy for alteration, and it correlates with the following textural changes: corroded rim and altered fractures where the growth zoning observed in pristine zircon is obliterated. In feldspar, sericitization and epidotization are extensive; however, the Na, Ca, and K contents are only slightly affected, and coherent REE patterns can be obtained for some grains. In amphibole, LREE losses in Sample MUS3 correlate with amphibole recrystallization as well as partial chloritization and biotitization.

In summary, the minerals of interest are slightly to strongly altered. As a result, only the amphibole, half of the apatite, and the zircon cores of Sample MUS7 may represent phases preserving magmatic domains. The other minerals, including the bulk of these observed in Samples MUS2 and MUS3, may have been altered too intensely to provide reliable estimates of primary physico-chemical parameters. Alteration explains that the $fO_2$, water content, P, and T obtained from the minerals of Sample MUS3 are systematically higher than those obtained from the amphibole, apatite, and zircon of Sample MUS7 (**Table 1**). As these samples come from co-magmatic intrusions having similar Si contents, similar physico-chemical parameters are expected.

The U-Pb isotope systematics may also have been locally affected by secondary processes. For example, the LA-ICP-MS ages obtained from the altered MUS3 dyke are 20 Ma older than those obtained using the more reliable ID-TIMS method (**Supplementary Materials S7, S8**). In addition, a significant proportion of the LA-ICP-MS ages obtained on zircons from the least-altered Sample MUS7 were discordant and rejected (**Figure 10**).

Discordance is likely due to alteration of high U domains and associated Pb-loss (lower Pb/U ages). Nonetheless, sufficiently pristine portions of MUS7 zircon grains yield concordant results that confirm a ca. 2701 Ma age for the Muscocho Pluton, and permit insight into the physico-chemical conditions of the studied magmatic system.

In summary, the in situ chemical analyses performed on the investigated Muscocho system minerals are strongly sensitive to hydrothermal alteration, and only the measurements performed on Sample MUS7 are representative of the conditions in which the studied magma evolved. This indicates that, even when considering the resistant zircon mineral, measurements performed in hydrothermally altered rocks, such as those that are spatially associated with IRGS, should always be interpreted with care.

### 5.4. Pressure, temperature, and magma ascent through the crust

As discussed in the previous section, only Sample MUS7 provides reliable indications of the physico-chemical conditions in which the Muscocho Pluton evolved and as such, only this sample is considered in this section. Amphibole and zircon may be relatively reliable, whereas—according to their textures and Na, Fe, and LREE contents—only half of the apatite of Sample MUS7 may be unaltered enough to provide reliable $fO_2$ data.

Apart from alteration, another source of uncertainty includes the parameters selected to calculate the physico-chemical data. For example, pressure and water content were evaluated using amphibole chemistry and a method (Ridolfi et al., 2010) formulated for amphiboles from calc-alkaline magmas observed in modern subduction settings. There is, however, no definite evidence for Neoarchean subduction (Mathieu et al., 2020b; Stern, 2005). Nonetheless, the studied magma has a major elements content akin to that of modern calc-alkaline melts. As the empirical formulations for temperature, water content, and $fO_2$ were deduced from the main constituent elements of amphibole, which is also dependent on magma composition (Ridolfi et al., 2010), the method may apply to the Muscocho Pluton, whether the magma was produced in a subduction setting or not.

In contrast, pressure estimates were calculated using the Al content of amphibole. The Mutch et al. (2016) method provides pressure estimates that are systematically twice that of the Ridolfi et al. (2010) approach for the studied rocks. The Ridolfi et al. (2010) barometric equation was retrieved from nine synthetic amphiboles, whereas the Mutch et

al. (2016) expression was formulated using a compilation of natural and experimental data from granitic rocks, and this approach was particularly well characterized for low-P conditions (as low as 0.5 kbar). We therefore consider that the Al-in-hornblende geobarometer calibration of Mutch et al. (2016) may best apply to the Muscocho intrusion. According to this barometer, most amphibole formed at about 4.5 kbar (**Table 1**), i.e., approximately 17-km continental depth equivalent. The rim of one amphibole that is in contact with oligoclase returned a pressure of 3.2 kbar; this value likely approximates the pressure at which sub-solidus reactions occurred. This indicates that the Muscocho Pluton may have been emplaced at about 12-km depth.

According to phase relations in the 'haplogranite' system of quartz-albite-orthoclase for water-saturated conditions (Tuttle and Bowen, 1958), the Muscocho Pluton contains too little quartz to have been produced by fractional crystallization at low pressure. After correcting for anorthite (Blundy and Cashman, 2001), the normative minerals lie close to the quartz-feldspar cotectic at 10 kbar (**Figure 2d**). In addition, magmatic epidote crystallised early, possibly together with amphibole (**Figure 4d**). Early epidote fractionation is promoted by elevated $fO_2$ and pressure in excess of 10 kbar (Schmidt and Poli, 2004; Zen and Hammarstrom, 1984). Discrepancy between epidote crystallisation pressure and intrusion emplacement pressure, as is observed for the Muscocho Pluton, is not unusual for granodiorite (Schmidt and Poli, 2004). These likely indicates that epidote crystallised at depth and that feldspar and the largest quartz grains started crystallizing at depth possibly during the progressive ascent of the magma through the crust (**Figure 11**). The Muscocho Pluton evolved as a relatively closed system and was likely emplaced as a crystal mush.

Another source of uncertainty is that, in the absence of melt inclusions and volcanic rocks related to the Muscocho Pluton, the chemical composition of the magma is unknown. Because of extensive alteration, the matrix of the MUS2 and MUS3 dykes was not used to approximate melt composition. Thus, to retrieve temperature and $fO_2$ from zircon chemistry, whole-rock analyses are assumed to be rough approximation of melt composition. However, the Muscocho Pluton contains large euhedral plagioclase, epidote, amphibole, and ± quartz that likely crystallized within a range of P conditions prior to

zircon-saturation. Whole rock chemistry is thus unlikely to be representative of the composition of the melt with which zircon equilibrated.

To evaluate the extent of this uncertainty, the model Si and K contents of the melt were increased arbitrarily. This increase had little effect on the $fO_2$ calculated from zircon (Smythe and Brenan, 2016) and had no effect on temperature estimates. Changing the composition of the melt, however, increased the $a_{TiO2}$ parameter. Increasing this parameter from 0.58 to 0.70 increased the $\log(fO_2)$ and temperature parameters of 0.5 and 20 °C, respectively. Ideally, the composition of the magma that equilibrated with zircon should be analysed using melt inclusions, which have not yet been found in the studied zircon. Although the errors on the temperature and $fO_2$ calculations are not well constrained, we consider the parametric estimates to be reasonably accurate.

Zircon may also provide unreliable information if inherited zircon are accidentally included into the dataset. The studied zircon, however, have a similar aspect ratio and texture in individual samples and provide temperature and $fO_2$ estimates that vary only within a narrow range. As demonstrated earlier, the ID-TIMS U-Pb data for Sample MUS3 revealed a very homogeneous population of 2700.2 ± 1.6 Ma grains, with no evidence of xenocrystic inheritance, while in situ LA-ICP-MS spot analyses of zircon from Sample MUS7 also gave equivalent magmatic ages, within error, at 2701 ± 5 Ma. We conclude that there is no evidence for inherited zircon being included in the determination of the T and $fO_2$ parameters in the studied rocks.

Altered zircon was discriminated readily from the dataset, based upon elevated La abundance (>0.1 ppm)—temperature and $fO_2$ deduced from grains with these levels were considered unreliable. Unaltered zircon crystallized at roughly 710 °C in the studied rocks, while the magma may have become Zr-saturated at approximately 1030 °C. These results point to a temperature difference (ΔT) of about 300 °C between Zr-saturation and the onset of zircon crystallization.

Despite the limitations listed above, the temperatures calculated using amphibole, zircon, and quartz decrease from 900 °C to 620 °C. This evolution of temperature is consistent with the crystallization sequence deduced from petrographic observations (**Figure 4**). The temperature calculated from quartz is, however, below the solidus temperatures for water-

saturated haplogranite (Holtz and Johannes, 1994; Mutch et al., 2016), which are 650 °C and 660 °C at 4.5 kbar and 3.2 kbar, respectively. There may be two reasons for this discrepancy: 1) the studied magma is not haplogranitic as it contains significant amounts of Ca-Mg-Fe, and the solidus temperature estimates are unreliable; and 2) quartz was deformed after the Muscocho Pluton had solidified—they also likely re-equilibrated in sub-solidus conditions—and the temperature measured from quartz may not correspond to the temperature at which this mineral crystallized in the magma. Given the abundance of subgrains observed in quartz, the latter hypothesis is considered likely.

Other mineral chemistry-based calculations indicate that the Muscocho magma likely started crystallizing during its ascent toward the upper crust. Feldspar ± quartz crystallization likely started at about 10 kbar (**Figure 2d**), while amphibole ± epidote crystallization may have initiated at a similar or higher pressure (Blundy and Cashman, 2001; Schmidt and Poli, 2004; Yoder and Tilley, 1962). Given a water content of 4.7 wt.% $H_2O$ (estimated using amphibole chemistry, Sample MUS7) and considering the haplogranite system as an analogue for the studied magma (Holtz et al., 2001), the crystallization of feldspar would have initiated at ~850 °C, a temperature that is within the upper range of temperatures measured from the amphibole observed in the studied rocks. These minerals are Fe-rich amphiboles and are unlikely to be representative of the first amphiboles that crystallized in the primitive magma, which was likely more Mg-rich (Krawczynski et al., 2012).

The studied magma that ascended to form the Muscocho Pluton is thus likely a differentiated melt. Progressive ascent of the magma under relatively isothermal conditions would have induced small temperature differences with the liquidus, i.e., undercooling or $\Delta T$. Crystallization under limited $\Delta T$ conditions promoted crystal growth over nucleation, leading to the formation of large, euhedral, epidote, feldspar, amphibole, and quartz minerals (**Figure 11**).

In the studied rocks, orthoclase and some quartz crystallized late as abundant minerals that are significantly smaller than the earlier, porphyritic plagioclase and amphibole crystals. Nucleation, in the latest stage of crystallization, was likely promoted by a large $\Delta T$. A large $\Delta T$ of about 300 °C was also recorded by zircon (see above). The large $\Delta T$ was likely

induced by a sudden pressure drop and/or by volatile exsolution (**Figure 11**). A sudden volatile release at about 3.2 kbar would have promoted crystallization, and the solidus may have been crossed at about 660 °C, analogous to the haplogranite system (Holtz et al., 2001; Holtz and Johannes, 1994). Volatile exsolution would also have increased viscosity dramatically and prevented the magma from raising to shallower levels.

By analogy with modern porphyry systems (Richards, 2009; Sillitoe, 2010), 12 km is too deep for an efficient hydrothermal system to initiate from magmatic fluids. The slow ascent of a water-rich (4.7 wt.% $H_2O$ or more) magma may have promoted volatile exsolution at depth, thus preventing the ascent of a volatile-rich magma to a shallow depth. This is possibly the primary reason for the lack of significant Au or Cu-Au magmatic-hydrothermal mineralization associated with the Muscocho Pluton.

### 5.5. Oxidation state

The oxidation state of the Muscocho Pluton magma was estimated using apatite, amphibole, and zircon chemistry. The measured $fO_2$ values are close to NNO, as is generally the case for calc-alkaline plutons (Holtz and Johannes, 1994; Johannes and Holtz, 1996; Mutch et al., 2016).

The Mn-in-apatite method (Miles et al., 2014) is likely the least reliable approach as it provides similar $fO_2$ estimates for Samples MUS3 and MUS7, whereas all other methods point to different oxidizing conditions in these samples (**Table 1**). The effect of manganese diffusion on calculated $fO_2$ is discussed in detail elsewhere (Miles et al., 2014), but given the size of the apatite analysed in the present study, this is considered minimal. This method does not provide a temperature estimate for apatite, and the results are thus difficult to compare with those obtained from amphibole and zircon. The Eu anomaly observed in apatite points to the lowest oxidizing conditions for the unaltered apatite of Sample MUS7, which is consistent with the $fO_2$ estimates obtained using zircon (**Table 1**).

Zircons that contain <0.1 ppm La point to moderately oxidizing $fO_2$ conditions of about NNO for Sample MUS7 and to more oxidizing conditions (NNO+1.45) for Sample MUS3. Amphibole provides the opposite results, with NNO and NNO+1 estimates for Samples MUS3 and MUS7, respectively (**Table 1**). Using zircon, $fO_2$ is estimated on the basis of the Eu and Ce anomalies and requires melt composition (including water content),

temperature, and $a_{TiO2}$ estimates (Smythe and Brenan, 2016). Using amphibole, $fO_2$ is estimated on the basis of the Mg, Si, Al, Ti, Fe, Ca, and Na content of the mineral (Ridolfi et al., 2010). Although both techniques have limitations, as discussed above, they provide similar results (within the error range). The $fO_2$ for the Muscocho Pluton (Sample MUS7) was thus likely about NNO+1 ±1.

Experimental studies suggest that Au solubility in magma is dependent on the S and/or Cl content of the melt and is optimal at FMQ+1 conditions (Botcharnikov et al., 2011), which is equivalent to NNO +0.34 to +0.76, whether the low-T or high-T FMQ buffers are considered. The Muscocho Pluton is thus slightly too oxidized to optimally transport Au. However, considering that $fO_2$ increases during differentiation (Middlemost, 1989) and given that the studied rocks are felsic, less differentiated intermediate magmas may have had an $fO_2$ that was more optimal for Au transportation.

Further investigations beyond the scope of this paper could provide estimates of the Cl and S contents of the studied magma, since Au solubility also depends on the activity of volatiles (Botcharnikov et al., 2011). Efforts should also be made to evaluate the metal content of this magma as, even under the most favourable conditions, magmas can only dissolve Au and base metals if these elements are available at the source. On the basis of the whole-rock analyses, the Muscocho Pluton contains a maximum of 6 ppb Au (and <2 ppb Au for most analyses); these values lie within the range of bulk crustal composition (Wedepohl, 1995), and the studied system does not seem to be particularly Au-rich. Specifying the volatile activity and metal content in the studied magma and other syntectonic intrusions will, however, require investigations of melt and sulphide micro-inclusions, which have not been observed in the samples presented here, and whose analysis is expected to be particularly challenging in Archean magmas.

## 6. Conclusions

The Muscocho Pluton is one of many granodiorite intrusions formed during the syntectonic period in the Abitibi Subprovince. It may be genetically related to significant magmatic-hydrothermal Au-mineralizing systems (IRGS) and detailed metallogeny studies focused on the spatially-associated Lac Muscocho and Lac Muscocho-Nord prospects, currently beyond the scope of this study, are necessary to confirm this point. This study shows that

the Muscocho Pluton is a simple, chemically and petrologically homogeneous intrusion. This ca. 2.70 Ga pluton is relatively undeformed, while its dykes are foliated, indicating that it emplaced toward the end of the $D_2$ phase, or between the $D_2$ and $D_3$ deformation phases, toward the end of the regional syntectonic period.

Crystallisation initiated at depth (pressure of 10 kbar at least, possibly more) and likely continued as the magma ascended through the crust. The magma was likely emplaced initially as a crystal mush with an undetermined proportion of interstitial melt. It is also concluded that the differentiated magma was slightly too oxidized to optimally transport Au. In addition, the magma did not rise to sufficiently shallow crustal levels to produce fluids capable of initiating a magmatic-hydrothermal system. Volatile exsolution at depth increased the viscosity of the magma and prevented its migration above 12-km depth. The reason for the magma emplacement at about 12-km depth is either due to volatile abundance or slow ascent, both of which can promote deep volatile exsolutions.

This study also shows that the Muscocho Pluton originated from a potentially metal-bearing source (metasomatized mantle). The crustal extent of the studied magmatic system is unconstrained. It also remains uncertain whether less differentiated parts of the magmatic system had the capacity (e.g., favourable $fO_2$) to transport significant amounts of Au, base metals, Cl, and F through the crust, toward the end of the syntectonic period. Evaluating the Cu-Au content of Neoarchean magmas will require dedicated studies and adapted analytical techniques. Modification of the LA-ICP-MS analytical parameters may provide more reliable results of the Au content of minerals. Also, measurements of melt inclusions could provide more direct and meaningful insight into magma composition. Adapting melt inclusion analyses to metamorphosed and ±altered ancient rocks is beyond the scope of this paper and should be the focus of future dedicated studies.

**Acknowledgments**

We extend thanks to Editor-in-Chief H. Chen and Associate Editor Z. Zhang, and to F. Leclerc and an anonymous reviewer, who greatly contributed to improve the quality of this manuscript. Warm thanks are addressed to P. Houle (MERN) and the summer 2018 mapping team of the Chibougamau transect (Metal Earth project): P. Bedeaux, M. Kieffer, J. Huguet, A. Boucher, A. Brochu, Y.A. Youssoufou, L.P. Perron-Desmeules, M.

Bellemare, and M. Desrochers. Many thanks to M. Choquette and S. Côté who operated the microprobe and the SEM at Laval University, and to D. Savard and A. Lavoie who provided technical support during use of the LA-ICP-MS of LabMaTer. The authors are indebted to the many collaborators of the Metal Earth project, including R. Sherlock, H. Gibson, B. Lafrance, P.C. Thurston, J. Ayer, D.J. Kontak, P. Bédard, and R. Daigneault. This paper is Metal Earth contribution number MERC-ME-2020-008.

This study was undertaken as part of the Metal Earth project (Laurentian University) investigation of the Chibougamau area. This research was funded by the Canada First Research Excellence Funds and federal/provincial/industry partners (http://merc.laurentian.ca/research/metal-earth/). This project was also funded by the NSERC (Natural Sciences and Engineering Research Council) Discovery Grant to L. Mathieu (Reference number RGPIN-2018-06325).

**Availability of data and material:** the bulk of data generated as part of this study are available as supplementary material, and include: 1) field photographs; 2) photomicrographs of minerals observed in natural and polarized lights; 3) whole rock analyses and sample list; 4) images of zircon grains and time-resolved LA-ICP-MS profiles; 5) microprobe analyses; 6) LA-ICP-MS analyses (trace elements); 7) LA-ICP-MS analyses (U-Pb analyses); and 8) ID-TIMS analyses (geochronology, Sample MUS3).

## Table Captions

**Table 1:** Summary of physico-chemical parameters for the Muscocho Pluton

[footnote – table 1] The methods used are: 1) (Hayden and Watson, 2007); 2) (Middlemost, 1989); 3, 7, 8, 11) (Ridolfi et al., 2010); 4) (Miles et al., 2014); 5) (Azadbakht et al., 2018); 6, 12) (Smythe and Brenan, 2016); 9) (Mutch et al., 2016); 10) (Watson and Harrison, 1983); 13) (Wark and Watson, 2006).

## Figure Captions

**Figure 1:** Geological map of the Chibougamau area showing the main volcanic, sedimentary, and intrusive units. Modified from the Ministère de l'Énergie et des Ressources Naturelles (MERN), Québec (SIGEOM, 2020). The projection is UTM

NAD83 Zone 18 N. Detailed map (figure inset) of the Muscocho Pluton area with location of samples collected during this study and samples compiled from the SIGEOM database.

**Figure 2:** Whole-rock ($n$ = 12) analyses displayed on (a) a total alkali silicate (TAS) diagram for intrusive rocks (Middlemost, 1985) and (b) a Na-K-Ca (wt.%) ternary diagram. The grey fields correspond to TTG suites compiled by (Moyen, 2019). Normative minerals are displayed on (c) a quartz-alkali feldspar-plagioclase (Q-A-P) diagram (Streckeisen, 1979) with the arrow illustrating the medium-K calc-alkaline trend (Lameyre and Bowden, 1982) and (d) a quartz-albite-orthoclase (in weight fraction units) ternary diagram for haplogranite with the positions of water-saturated quartz+feldspar cotectics labelled with pressure (Johannes and Holtz, 1996). The haplogranite system is eutectic at 10 kbar. The data were projected onto the ternary diagram by accounting for the anorthite component (Blundy and Cashman, 2001). On most diagrams, the dykes are off-trend due to mass changes induced by hydrothermal alteration. Additional diagrams are available in supplementary material S3D.

**Figure 3:** Whole rock analyses displayed on (a) a multielement arachnid diagram (Pearce, 2008) and (b) a REE diagram. Rocks are normalized to the primitive mantle (Hofmann, 1988).

**Figure 4:** (a) Sample MUS7 and (d, e) sample D83-131A observed under natural light; (b, c) samples MUS3 and MUS2 observed under polarized light. (f) Interpreted and simplified mineralogy as detected semi-automatically using natural light images of thin sections from the Muscocho Pluton. Mineral abbreviations are as reported in the literature (Whitney and Evans, 2010).

**Figure 5:** (a) Sample MUS7 observed under cathodoluminescence and showing the distribution of orthoclase in and around quartz grains, as well as the spatial association between apatite and amphibole. (b) Zircon from Sample MUS7 observed using backscattered electrons (BSE), cathodoluminescence (CL), and natural light (NL). Mineral abbreviations are as reported in the literature (Whitney and Evans, 2010).

**Figure 6:** (a) Feldspar chemistry displayed in feldspar ternary diagram ($n$ = 54). Apatite chemistry displayed in (b) Cl-F-S ternary diagram ($n$ = 73), (c) Mn-Na-Ca ternary diagram ($n$ = 104), and (d) Mn-Fe-Ca ternary diagram ($n$ = 104). In the lower diagrams (c, d), the

field is for apatite observed in low-temperature hydrothermal systems (Camprubí et al., 2018; Dorais et al., 1997; Piccoli and Candela, 2002), while apatite having low Fe and Na contents are from magmatic systems.

**Figure 7:** REE diagrams normalized to the primitive mantle (Hofmann, 1988) displaying LA-ICP-MS results for (a) feldspar ($n$ = 32), (b) amphibole ($n$ = 48), (c) apatite ($n$ = 31), and (d) zircon ($n$ = 227).

**Figure 8:** Diagrams of (a) pressure vs temperature, (b) oxidation state vs temperature, and (c) temperature vs water content of the magma, all deduced from the chemistry of amphibole (Ridolfi et al., 2010). On these diagrams, the crosses correspond to (a) the maximum depth uncertainties, calculated using a crust specific weight of 2.7 g/cm$^3$ and (c) the maximum relative error for water content (15%, black error bars) and temperature (0.4 wt.%, blue error bar) (Ridolfi et al., 2010). (d) Oxidation state deduced from apatite chemistry displayed on the Eu vs Ce anomaly diagram for apatite (Azadbakht et al., 2018). The (e) La vs temperature and (f) La vs oxidation state diagrams use parameters calculated from zircon (Smythe and Brenan, 2016).

**Figure 9:** Concordia diagram showing results of conventional ID-TIMS analyses carried out on zircon from Sample MUS3. Three single zircon grains (Z1, Z2, and Z3) were analysed, yielding a weighted average $^{207}Pb/^{206}Pb$ age of 2700.2 ± 1.6 Ma (MSWD, mean square of the weighted deviates = 0.21, and a probability of fit of 81%). Error ellipses and age errors are shown at the 2 sigma level of uncertainty.

**Figure 10:** Results of LA-ICP-MS analyses performed on zircon and displayed on the weighted mean diagram for Sample MUS7. $^{207}Pb/^{206}Pb$ ages are provided as weighted mean age ± 1σ (standard error) and are calculated for concordant analyses (Concordia diagrams available in **Supplementary Material S7**). The MSWD parameter is >1, indicating that the ages are overdispersed with respect to the stated analytical uncertainties, and the $p(X^2)$, the Chi-square probability, is >0.05, indicating that overdispersion is limited for concordant analyses.

**Figure 11:** Schematic isothermal decompression path for the magma of the Muscocho Pluton and related dykes, inspired by the model proposed for a Mount St Helens dacite (Blundy and Cashman, 2001). The diagram shows several ascent steps from depth,

associated with undercooling (ΔT) relative to the liquidus at the appropriate pressure. Slow ascent promotes a small ΔT, limited nucleation, and crystal growth to form large euhedral plagioclase, quartz, and amphibole, whereas a large ΔT promotes crystal nucleation and limited growth to form small alkali feldspar and quartz. This simplified representation assumes that, after each ascent step, crystallization has sufficient time to reduce the liquidus to the isotherm (Blundy and Cashman, 2001).

## References


Allard, G.O., 1976. Doré Lake Complex and its importance to Chibougamau Geology and Metallogeny. MRN report DPV-386, Ministère des Ressources Naturelles: Québec, QC, Canada.

Azadbakht, Z., Lentz, D., McFarlane, C., 2018. Apatite Chemical Compositions from Acadian-Related Granitoids of New Brunswick, Canada: Implications for Petrogenesis and Metallogenesis. Minerals 8, 598.

Barker, D.S., 1978. Magmatic trends on alkali-iron-magnesium diagrams. Am. Mineral. 63, 531–534.

Bateman, R., Ayer, J.A., Dubé, B., Hamilton, M.A., 2005. The Timmins-Porcupine Gold Camp, Northern Ontario: The anatomy of an Archaean greenstone belt and its gold mineralization: Discover Abitibi Initiative. Ontario Geological Survey, Open File report 6158.

Bédard, L.P., 1996. Archean high-Mg quartz-monzodiorite suite: a re-evaluation of the parental magma and differentiation. J. Geol. 104, 713–728.

Blundy, J., Cashman, K., 2001. Ascent-driven crystallisation of dacite magmas at Mount St Helens, 1980-1986. Contrib. to Mineral. Petrol. 140, 631–650.

Botcharnikov, R.E., Linnen, R.L., Holtz, F., 2010. Solubility of Au in Cl-and S-bearing hydrous silicate melts. Geochim. Cosmochim. Acta 74, 2396–2411.

Botcharnikov, R.E., Linnen, R.L., Wilke, M., Holtz, F., Jugo, P.J., Berndt, J., 2011. High gold concentrations in sulphide-bearing magma under oxidizing conditions. Nat. Geosci. 4, 112.

Cameron, E.M., Hattori, K., 1987. Archean gold mineralization and oxidized hydrothermal fluids. Econ. Geol. 82, 1177–1191.

Camprubí, A., Centeno-García, E., Tolson, G., Iriondo, A., Ortega, B., Bolanos, D., Abdullin, F., Portugal-Reyna, J.L., Ramos-Arias, M.A., 2018. Geochronology of Mexican mineral deposits. VII: the Peña Colorada magmatic-hydrothermal iron oxide deposits (IOCG "clan"), Colima. Boletín la Soc. Geol. Mex. 70, 633–674.

Daigneault, R., 1991. Évolution structurale du segment de roches vertes de Chibougamau, Sous-province archéenne de l'Abitibi, Québec. Unpublished PhD thesis, Laval University, Québec, QC, Canada.

Daigneault, R., Allard, G.O., 1990. Le Complexe du lac Doré et son environnement géologique (région de Chibougamau-sous-province de l'Abitibi). MRN report MM-89-03, Ministère des Ressources Naturelles: Québec, QC, Canada.

Daigneault, R., St-Julien, P., Allard, G.O., 1990. Tectonic evolution of the northeast portion of the Archean Abitibi greenstone belt, Chibougamau area, Quebec. Can. J. Earth Sci. 27, 1714–1736.

Dallmeyer, R.D., Maybin, A.H., Durocher, M.E., 1975. Timing of Kenoran Metamorphism in the Eastern Abitibi Greenstone Belt, Quebec: Evidence From 40Ar/39Ar Ages of Hornblende and Biotite From Post-Kinematic Plutons. Can. J. Earth Sci. 12, 1864–1873.

David, J., Simard, M., Bandyayera, D., Goutier, J., Hammouche, H., Pilote, P., Leclerc, F., Dion, C., 2012. Datations U-Pb effectuées dans les provinces du Supérieur et de Churchill en 2010-2011. MRNF report RP-2012-01; Ministère des Ressources Naturelles et de la Faune: Québec, QC, Canada.

David, J., Vaillancourt, D., Bandyayera, D., Simard, M., Goutier, J., Pilote, P., Dion, C., Barbe, P., 2011. Datations U-Pb Effectuées dans les Sousprovinces d'Ashuanipi, de La Grande, d'Opinaca et d'Abitibi en 2008-2009. MERN report, RP-2010-11; Ministère de l'Énergie et des Ressources Naturelles: Québec, QC, Canada.

Davis, D., David, J., Dion, C., Goutier, J., Bandyayera, D., Rhéaume, P., Roy, P., 2005. Datations U-Pb effectuées en support aux travaux de cartographie géologique et de compilation géoscientifique du SGNO (2003-2004). MRNF report RP 2005-02; Ministère des Ressources Naturelles et de la Faune: Québec, QC, Canada.

Davis, W.J., Machado, N., Gariépy, C., Sawyer, E.W., Benn, K., 1995. U-Pb geochronology of the Opatica tonalite-gneiss belt and its relationship to the Abitibi greenstone belt, Superior Province, Quebec. Can. J. Earth Sci. 32, 113–127.

De Souza, S., Dubé, B., McNicoll, V.J., Dupuis, C., Mercier-Langevin, P., Creaser, R.A., Kjarsgaard, I.M., 2015. Geology, hydrothermal alteration, and genesis of the world-class Canadian Malartic stockwork-disseminated Archean gold deposit, Abitibi, Quebec, in: Dubé, B., Mercier-Langevin, P. (Eds.), Targeted Geoscience Initiative 4: Contributions to the Understanding of Precambrian Lode Gold Deposits and Implications for Exploration. Geological Survey of Canada, Open File 7852, pp. 113–126.

Dorais, M.J., Lira, R., Chen, Y., Tingey, D., 1997. Origin of biotite-apatite-rich enclaves, Achala batholith, Argentina. Contrib. to Mineral. Petrol. 130, 31–46.

Drake, M.J., Weill, D.F., 1975. Partition of Sr, Ba, Ca, Y, Eu2+, Eu3+, and other REE between plagioclase feldspar and magmatic liquid: an experimental study. Geochim. Cosmochim. Acta 39, 689–712.

Faure, S., 2015. Relations entre les minéralisations aurifères et les isogrades métamorphiques en Abitibi / Relationship between gold mineralisations and metamorphic isograde in Abitibi [online]. Consorem project 2013-03, available at: http://www.consorem.ca/rapports_publics.html (accessed on 10th of august 2018).

Fayol, N., Jébrak, M., 2017. Archean sanukitoid gold porphyry deposits: a new

understanding and genetic model from the Lac Bachelor gold deposit, Abitibi, Canada. Econ. Geol. 112, 1913–1936.

Feng, R., Kerrich, R., 1992. Geochemical evolution of granitoids from the Archean Abitibi Southern Volcanic Zone and the Pontiac subprovince, Superior Province, Canada: implications for tectonic history and source regions. Chem. Geol. 98, 23–70.

Ferry, J.M., Watson, E.B., 2007. New thermodynamic models and revised calibrations for the Ti-in-zircon and Zr-in-rutile thermometers. Contrib. to Mineral. Petrol. 154, 429–437.

Gariépy, C., Allègre, C.J., 1985. The lead isotope geochemistry and geochronology of late-kinematic intrusives from the Abitibi greenstone belt, and the implications for late Archaean crustal evolution. Geochim. Cosmochim. Acta 49, 2371–2383.

Gerstenberger, H., Haase, G., 1997. A highly effective emitter substance for mass spectrometric Pb isotope ratio determinations. Chem. Geol. 136, 309–312.

Gosselin, P., Dubé, B., 2005. Gold deposits of the world: distribution, geological parameters and gold content. Geological Survey of Canada Open File 4895.

Groves, D.I., Goldfarb, R.J., Gebre-Mariam, M., Hagemann, S.G., Robert, F., 1998. Orogenic gold deposits: a proposed classification in the context of their crustal distribution and relationship to other gold deposit types. Ore Geol. Rev. 13, 7–27.

Hawthorne, F.C., Oberti, R., Harlow, G.E., Maresch, W. V, Martin, R.F., Schumacher, J.C., Welch, M.D., 2012. Nomenclature of the amphibole supergroup. Am. Mineral. 97, 2031–2048.

Hayden, L.A., Watson, E.B., 2007. Rutile saturation in hydrous siliceous melts and its bearing on Ti-thermometry of quartz and zircon. Earth Planet. Sci. Lett. 258, 561–568.

Helt, K., 2012. The Canadian Malartic Deposit: An Example of Oxidized, Intrusion-related Gold Mineralization in the Abitibi Greenstone Belt, Québec, Canada. Unpublished Master thesis, McGill University, Montréal, QC, Canada.

Higgins, M.D., van Breemen, O., 1998. The age of the Sept Iles layered mafic intrusion, Canada: implications for the late Neoproterozoic/Cambrian history of southeastern Canada. J. Geol. 106, 421–432.

Hofmann, A.W., 1988. Chemical differentiation of the Earth: the relationship between mantle, continental crust, and oceanic crust. Earth Planet. Sci. Lett. 90, 297–314.

Holtz, F., Becker, A., Wilhelm, J., 2001. The water-undersaturated and dry Qz-Ab-Or system revisited. Experimental results at very low water activities and geological implications. Contrib. to Mineral. Petrol. 141, 347.

Holtz, F., Johannes, W., 1994. Maximum and minimum water contents of granitic melts: implications for chemical and physical properties of ascending magmas. Lithos 32, 149–159.

Ispolatov, V., Lafrance, B., Dubé, B., Creaser, R., Hamilton, M., 2008. Geologic and

structural setting of gold mineralization in the Kirkland Lake-Larder Lake gold belt, Ontario. Econ. Geol. 103, 1309–1340.

Jensen, E.P., Barton, M.D., 2000. Gold Deposits Related to Alkaline Magmatism, in: Hagemann, S.G., Brown, P.E. (Eds.), Gold in 2000. Society of Economic Geologists, Littleton, Colorado, USA, pp. 279–314.

Jochum, K.P., Nohl, U., Herwig, K., Lammel, E., Stoll, B., Hofmann, A.W., 2005a. GeoReM: a new geochemical database for reference materials and isotopic standards. Geostand. Geoanalytical Res. 29, 333–338.

Jochum, K.P., Weis, U., Stoll, B., Kuzmin, D., Yang, Q., Raczek, I., Jacob, D.E., Stracke, A., Birbaum, K., Frick, D.A., 2011. Determination of reference values for NIST SRM 610-617 glasses following ISO guidelines. Geostand. Geoanalytical Res. 35, 397–429.

Jochum, K.P., Willbold, M., Raczek, I., Stoll, B., Herwig, K., 2005b. Chemical Characterisation of the USGS Reference Glasses GSA 1G, GSC 1G, GSD 1G, GSE 1G, BCR 2G, BHVO 2G and BIR 1G Using EPMA, ID TIMS, ID-ICP-MS and LA-ICP-MS. Geostand. Geoanalytical Res. 29, 285–302.

Johannes, W., Holtz, F., 1996. Petrogenesis and experimental petrology of granitic rocks. Springer Science & Business Media.

Jolly, W.T., 1974. Regional metamorphic zonation as an aid in study of Archean terrains: Abitibi region, Ontario. Can. Mineral. 12, 499–508.

Katz, L.R., Kontak, D.J., Dubé, B., McNicoll, V., 2017. The geology, petrology, and geochronology of the Archean Côté Gold large-tonnage, low-grade intrusion-related Au (±Cu) deposit, Swayze greenstone belt, Ontario, Canada. Can. J. Earth Sci. 54, 173–202.

Klein, M., Stosch, H.-G., Seck, H.A., 1997. Partitioning of high field-strength and rare-earth elements between amphibole and quartz-dioritic to tonalitic melts: an experimental study. Chem. Geol. 138, 257–271.

Krawczynski, M.J., Grove, T.L., Behrens, H., 2012. Amphibole stability in primitive arc magmas: effects of temperature, H 2 O content, and oxygen fugacity. Contrib. to Mineral. Petrol. 164, 317–339.

Krogh, T.E., 1982. Improved accuracy of U-Pb zircon ages by the creation of more concordant systems using an air abrasion technique. Geochim. Cosmochim. Acta 46, 637–649.

Krogh, T.E., 1973. A low-contamination method for hydrothermal decomposition of zircon and extraction of U and Pb for isotopic age determinations. Geochim. Cosmochim. Acta 37, 485–494.

Lameyre, J., Bowden, P., 1982. Plutonic rock types series: discrimination of various granitoid series and related rocks. J. Volcanol. Geotherm. Res. 14, 169–186.

Lang, J.R., Baker, T., 2001. Intrusion-related gold systems: the present level of understanding. Miner. Depos. 36, 477–489.

Lawley, C., Kjarsgaard, B., Jackson, S., Yang, Z., Petts, D., Roots, E., 2018. Trace metal and isotopic depth profiles through the Abitibi cratonic mantle. Lithos 314, 520–533.

Le Bas, M.J., Le Maitre, R.W., Woolley, A.R., 1992. The construction of the total alkali-silica chemical classification of volcanic rocks. Mineral. Petrol. 46, 1–22. https://doi.org/10.1007/BF01160698

Le Maitre, R.W., Streckeisen, A., Zanettin, B., Le Bas, M.J., Bonin, B., Bateman, P., Bellieni, G., Dudek, A., Efremova, S., Keller, J., 2002. Igneous rocks: A classification and glossary of terms; Recommendations of the International Union of Geological Sciences, in: Subcommission on the Systematics of Igneous Rocks. Cambridge University Press, Cambridge, United Kingdom, p. 230.

Leake, B.E., Woolley, A.R., Arps, C.E.S., Birch, W.D., Gilbert, M.C., Grice, J.D., Hawthorne, F.C., Kato, A., Kisch, H.J., Krivovichev, V.G., 1997. Report. Nomenclature of Amphiboles: Report of the Subcommittee on Amphiboles of the International Mineralogical Association Commission on New Minerals and Mineral Names. Mineral. Mag. 61, 295–321.

Leclerc, F., Harris, L.B., Bédard, J.H., van Breemen, O., Goulet, N., 2012. Structural and Stratigraphic Controls on Magmatic, Volcanogenic, and Shear Zone-Hosted Mineralization in the Chapais-Chibougamau Mining Camp, Northeastern Abitibi, Canada. Econ. Geol. 107, 963–989.

Leclerc, F., Roy, P., Pilote, P., Bédard, J.H., Harris, L.B., McNicoll, V.J., Breemen, O. van, David, J., Goulet, N., 2017. Géologie de la Région de Chibougamau. MERN report RG 2015-03, Ministère de l'Énergie et des Ressources Naturelles: Québec, QC, Canada.

Levesque, G., 1994. Duality of magmatism at Kirkland Lake, Ontario, Canada. Unpublished Master thesis, Carlton University, Ottawa, ON, Canada.

Levesque, G.S., Cameron, E.M., Lalonde, A.E., 1991. Duality of magmatism along the Kirkland Lake-Larder Lake fault zone, Ontario. Curr. Res., Part C, Geol. Surv. Canada, Pap 17–24.

Ludwig, K.R., 2009. User's manual for Isoplot 3.71 a geochronological toolkit for Excel. Berkeley Geochronological Cent. Spec. Publ. 4, 72.

Mathieu, L., 2019. Origin of the Vanadiferous Serpentine-Magnetite Rocks of the Mt. Sorcerer Area, Lac Doré Layered Intrusion, Chibougamau, Québec. Geosciences 9, 110.

Mathieu, L., Crépon, A., Kontak, D.J., 2020a. Tonalite-Dominated Magmatism in the Abitibi Subprovince, Canada, and Significance for Cu-Au Magmatic-Hydrothermal Systems. Minerals 10, 242.

Mathieu, L., Racicot, D., 2019. Petrogenetic Study of the Multiphase Chibougamau Pluton: Archaean Magmas Associated with Cu-Au Magmato-Hydrothermal Systems. Minerals 9, 174.

Mathieu, L., Snyder, D.B., Bedeaux, P., Cheraghi, S., Lafrance, B., Thurston, P.,

Sherlock, R., 2020b. Deep into the Chibougamau area, Abitibi greenstone belt: structure of a Neoarchean crust revealed by seismic reflection profiling. Earth Sp. Sci. Open Arch. https://doi.org/10.1002/essoar.10501539.1

Mattinson, J.M., 2005. Zircon U-Pb chemical abrasion ('CA-TIMS') method: combined annealing and multi-step partial dissolution analysis for improved precision and accuracy of zircon ages. Chem. Geol. 220, 47–66.

McNicoll, V., Dubé, B., Goutier, J., Mercier-Langevin, P., Dion, C., Monecke, T., Ross, P.-S.–, Thurston, P., Pilote, P., Bédard, J., Leclerc, F., Bécu, V., Percival, J., Legault, M., Gibson, H., Ayer, J., 2008. Nouvelles datations U-Pb dans le Cadre du Projet ICG-3 Abitibi/Plan Cuivre : Incidences pour l'Interprétation Géologique et l'Exploration des Métaux Usuels. MRN report DV-2008-06; Ministère des Ressources Naturelles: Québec, QC, Canada.

Middlemost, E.A.K., 1989. Iron oxidation ratios, norms and the classification of volcanic rocks. Chem. Geol. 77, 19–26.

Middlemost, E.A.K., 1985. Naming materials in the magma/igneous rock system. Earth-Sciences Rev. 37, 215–224.

Miles, A.J., Graham, C.M., Hawkesworth, C.J., Gillespie, M.R., Hinton, R.W., Bromiley, G.D., 2014. Apatite: A new redox proxy for silicic magmas? Geochim. Cosmochim. Acta 132, 101–119.

Mortensen, J.K., 1993. U–Pb geochronology of the eastern Abitibi subprovince. Part 1: Chibougamau–Matagami–Joutel region. Can. J. Earth Sci. 30, 11–28.

Moyen, J.-F., 2019. Archean granitoids: classification, petrology, geochemistry and origin. Geol. Soc. London, Spec. Publ. 489, SP489-2018.

Moyen, J.-F., Martin, H., 2012. Forty years of TTG research. Lithos 148, 312–336.

Mutch, E.J.F., Blundy, J.D., Tattitch, B.C., Cooper, F.J., Brooker, R.A., 2016. An experimental study of amphibole stability in low-pressure granitic magmas and a revised Al-in-hornblende geobarometer. Contrib. to Mineral. Petrol. 171, 85.

Paton, C., Hellstrom, J., Paul, B., Woodhead, J., Hergt, J., 2011. Iolite: Freeware for the visualisation and processing of mass spectrometric data. J. Anal. At. Spectrom. 26, 2508–2518.

Pearce, J.A., 2008. Geochemical fingerprinting of oceanic basalts with applications to ophiolite classification and the search for Archean oceanic crust. Lithos 100, 14–48.

Phillips, G.N., Powell, R., 2010. Formation of gold deposits: a metamorphic devolatilization model. J. Metamorph. Geol. 28, 689–718.

Piccoli, P.M., Candela, P.A., 2002. Apatite in igneous systems. Rev. Mineral. Geochemistry 48, 255–292.

Piché, M., 1985. La formation de Haüy à l'ouest de Chapais; volcanisme sub-aérien en milieu fluviatile. Unpublished Master thesis, Université du Québec à Chicoutimi, Chicoutimi, QC, Canada.

Pilote, P., Dion, C., Joanisse, A., David, J., Machado, N., Kirkham, R. V, Robert, F.,

1997. Géochronologie des minéralisations d'affiliation magmatique de l'Abitibi, secteurs Chibougamau et de Troilus-Frotet: implications géotectoniques, in: Programme et Résumés, Séminaire d'information Sur La Recherche Géologique. MRN report, DV-97-03; Ministère des Ressources Naturelles: Québec, QC, Canada, p. 47.

Racicot, D., Chown, E.H., Hanel, T., 1984. Plutons of the Chibougamau-Desmaraisville Belt: A Preliminary Survey, in: Guha, J., Chown, E. (Eds.), Chibougamau, Stratigraphy and Mineralization. Canadian Institute of Mining and Metallurgy: Westmount, QC, Canada, pp. 178–197.

Richards, J.P., 2009. Postsubduction porphyry Cu-Au and epithermal Au deposits: Products of remelting of subduction-modified lithosphere. Geology 37, 247–250.

Ridolfi, F., Renzulli, A., Puerini, M., 2010. Stability and chemical equilibrium of amphibole in calc-alkaline magmas: an overview, new thermobarometric formulations and application to subduction-related volcanoes. Contrib. to Mineral. Petrol. 160, 45–66.

Robert, F., 2001. Syenite-associated disseminated gold deposits in the Abitibi greenstone belt, Canada. Miner. Depos. 36, 503–516.

Ross, P.-S., Bédard, J.H., 2009. Magmatic affinity of modern and ancient subalkaline volcanic rocks determined from trace-element discriminant diagrams. Can. J. Earth Sci. 46, 823–839.

Rowins, S.M., Lalonde, A.E., Cameron, E.M., 1991. Magmatic oxidation in the syenitic Murdock Creek intrusion, Kirkland Lake, Ontario: evidence from the ferromagnesian silicates. J. Geol. 99, 395–414.

Schmidt, M.W., Poli, S., 2004. Magmatic epidote. Rev. Mineral. Geochemistry 56, 399–430.

SIGEOM, 2020. Système d'information géominière du Québec [WWW Document]. Ministère l'Énergie des Ressources Nat. Québec, Canada. URL http://sigeom.mines.gouv.qc.ca (accessed 1.1.20).

SIGEOM, 2019a. Lac Muscocho-Nord showing file 32G/10-1003 [WWW Document]. URL http://sigeom.mines.gouv.qc.ca/signet/classes/I1103_index?format=COMPLET&type_reqt=U&mode=NOUVELLE&l=F&entt=GM&numr_utls=3187192&alias_table_crit=F4E02&mnen_crit=NUMR_INTER&oper_crit=EGAL&valr_crit=3809 (accessed 10.2.19).

SIGEOM, 2019b. Lac Muscocho showing file 32G/10-0019 [WWW Document]. URL http://sigeom.mines.gouv.qc.ca/signet/classes/I1103_index?format=COMPLET&type_reqt=U&mode=NOUVELLE&l=F&entt=GM&numr_utls=3187192&alias_table_crit=F4E02&mnen_crit=NUMR_INTER&oper_crit=EGAL&valr_crit=3798 (accessed 10.2.19).

Sillitoe, R.H., 2010. Porphyry copper systems. Econ. Geol. 105, 3–41.

Sláma, J., Košler, J., Condon, D.J., Crowley, J.L., Gerdes, A., Hanchar, J.M., Horstwood,

M.S.A., Morris, G.A., Nasdala, L., Norberg, N., 2008. Plesovice zircon-a new natural reference material for U-Pb and Hf isotopic microanalysis. Chem. Geol. 249, 1–35.

Smythe, D.J., Brenan, J.M., 2016. Magmatic oxygen fugacity estimated using zircon-melt partitioning of cerium. Earth Planet. Sci. Lett. 453, 260–266.

Stacey, J.S. t, Kramers, 1JD, 1975. Approximation of terrestrial lead isotope evolution by a two-stage model. Earth Planet. Sci. Lett. 26, 207–221.

Stern, R.A., Hanson, G.N., Shirey, S.B., 1989. Petrogenesis of mantle-derived, LILE-enriched Archean monzodiorites and trachyandesites (sanukitoids) in southwestern Superior Province. Can. J. Earth Sci. 26, 1688–1712.

Stern, R.J., 2005. Evidence from ophiolites, blueschists, and ultrahigh-pressure metamorphic terranes that the modern episode of subduction tectonics began in Neoproterozoic time. Geology 33, 557–560.

Streckeisen, A., 1979. Classification and nomenclature of volcanic rocks, lamprophyres, carbonatites, and melilitic rocks: Recommendations and suggestions of the IUGS Subcommission on the Systematics of Igneous Rocks. Geology 7, 331–335.

Sutcliffe, R.H., Barrie, C.T., Burrows, D.R., Beakhouse, G.P., 1993. Plutonism in the southern Abitibi Subprovince; a tectonic and petrogenetic framework. Econ. Geol. 88, 1359–1375.

Tait, L., 1992. Géologie de la région du lac à l'Eau Jaune (Territoire-du-Nouveau-Québec). MER report MB 91-29; Ministère de l'Énergie et des Ressources: Québec, QC, Canada.

Tuttle, O.F., Bowen, N.L., 1958. Origin of granite in the light of experimental studies in the system NaAlSiO8-KALSi3O8-SiO2-H2O. Geological Society of America.

Vermeesch, P., 2018. IsoplotR: a free and open toolbox for geochronology. Geosci. Front. 9, 1479–1493.

Wark, D.A., Watson, E.B., 2006. TitaniQ: a titanium-in-quartz geothermometer. Contrib. to Mineral. Petrol. 152, 743–754.

Watson, E.B., Harrison, T.M., 1983. Zircon saturation revisited: temperature and composition effects in a variety of crustal magma types. Earth Planet. Sci. Lett. 64, 295–304.

Wedepohl, K.H., 1995. The composition of the continental crust. Geochim. Cosmochim. Acta 59, 1217–1232.

Whitney, D.L., Evans, B.W., 2010. Abbreviations for names of rock-forming minerals. Am. Mineral. 95, 185–187.

Wiedenbeck, M., Hanchar, J.M., Peck, W.H., Sylvester, P., Valley, J., Whitehouse, M., Kronz, A., Morishita, Y., Nasdala, L., Fiebig, J., 2004. Further characterisation of the 91500 zircon crystal. Geostand. Geoanalytical Res. 28, 9–39.

Williams-Jones, A.E., Migdisov, A.A., Samson, I.M., 2012. Hydrothermal mobilisation of the rare earth elements-a tale of "ceria" and "yttria." Elements 8, 355–360.

Yoder, H.S., Tilley, C.E., 1962. Origin of basalt magmas: an experimental study of natural and synthetic rock systems. J. Petrol. 3, 342–532.

Zen, E.-A., Hammarstrom, J.M., 1984. Magmatic epidote and its petrologic significance. Geology 12, 515–518.

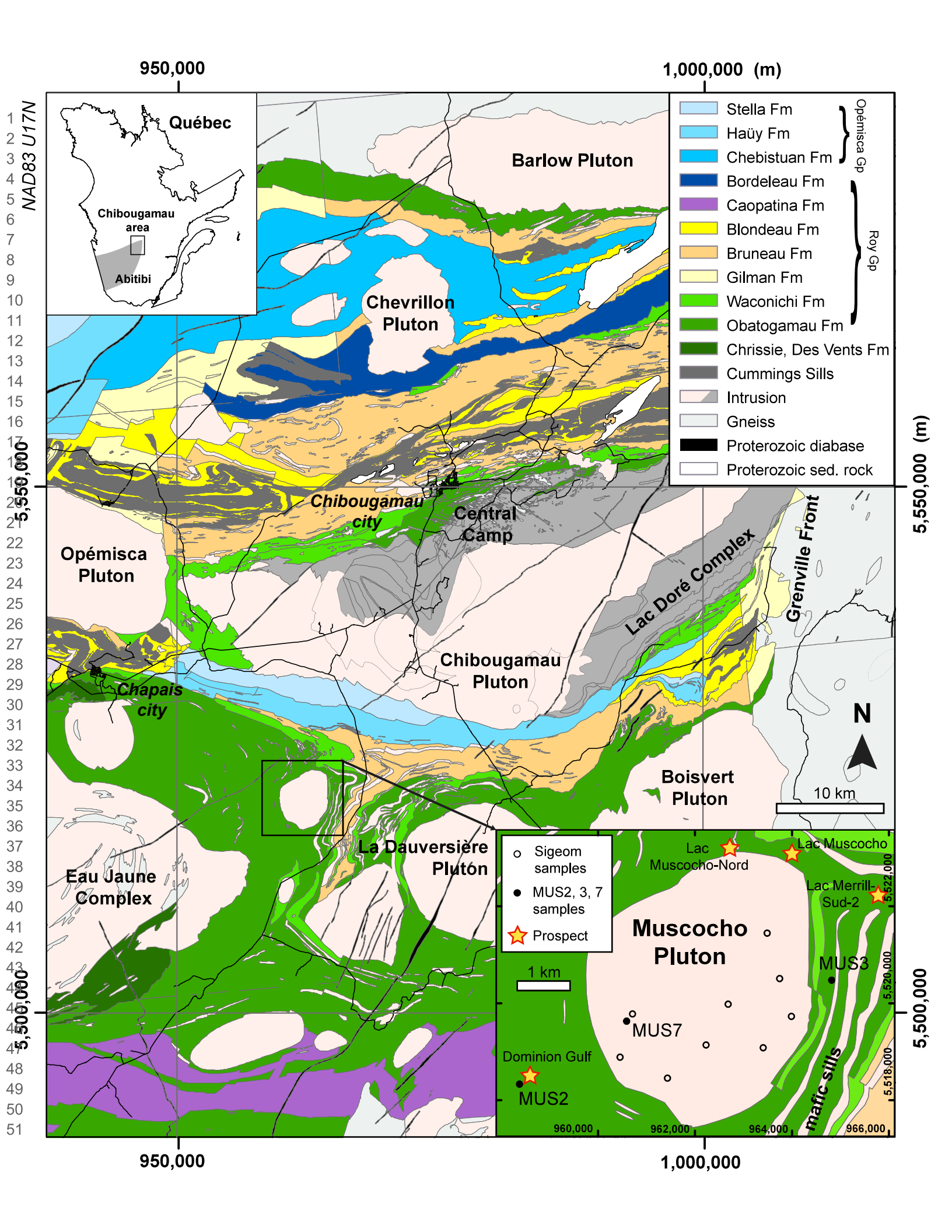
950,000
1,000,000 (m)
NAD83 U17N
5,550,000
5,550,000 (m)
5,500,000
5,500,000
950,000
1,000,000
Québec
Chibougamau area
Abitibi
Stella Fm
Haüy Fm
Chebistuan Fm
Opémisca Gp
Bordeleau Fm
Caopatina Fm
Blondeau Fm
Bruneau Fm
Gilman Fm
Waconichi Fm
Obatogamau Fm
Roy Gp
Chrissie, Des Vents Fm
Cummings Sills
Intrusion
Gneiss
Proterozoic diabase
Proterozoic sed. rock
Barlow Pluton
Chevrillon Pluton
Chibougamau city
Central Camp
Opémisca Pluton
Lac Doré Complex
Grenville Front
Chibougamau Pluton
Chapais city
Boisvert Pluton
N
10 km
La Dauversière Pluton
Eau Jaune Complex
Sigeom samples
MUS2, 3, 7 samples
Prospect
1 km
Lac Muscocho-Nord
Lac Muscocho
Lac Merrill-Sud-2
Muscocho Pluton
MUS3
MUS7
Dominion Gulf
MUS2
mafic sills
5,522,000
5,520,000
5,518,000
960,000
962,000
964,000
966,000

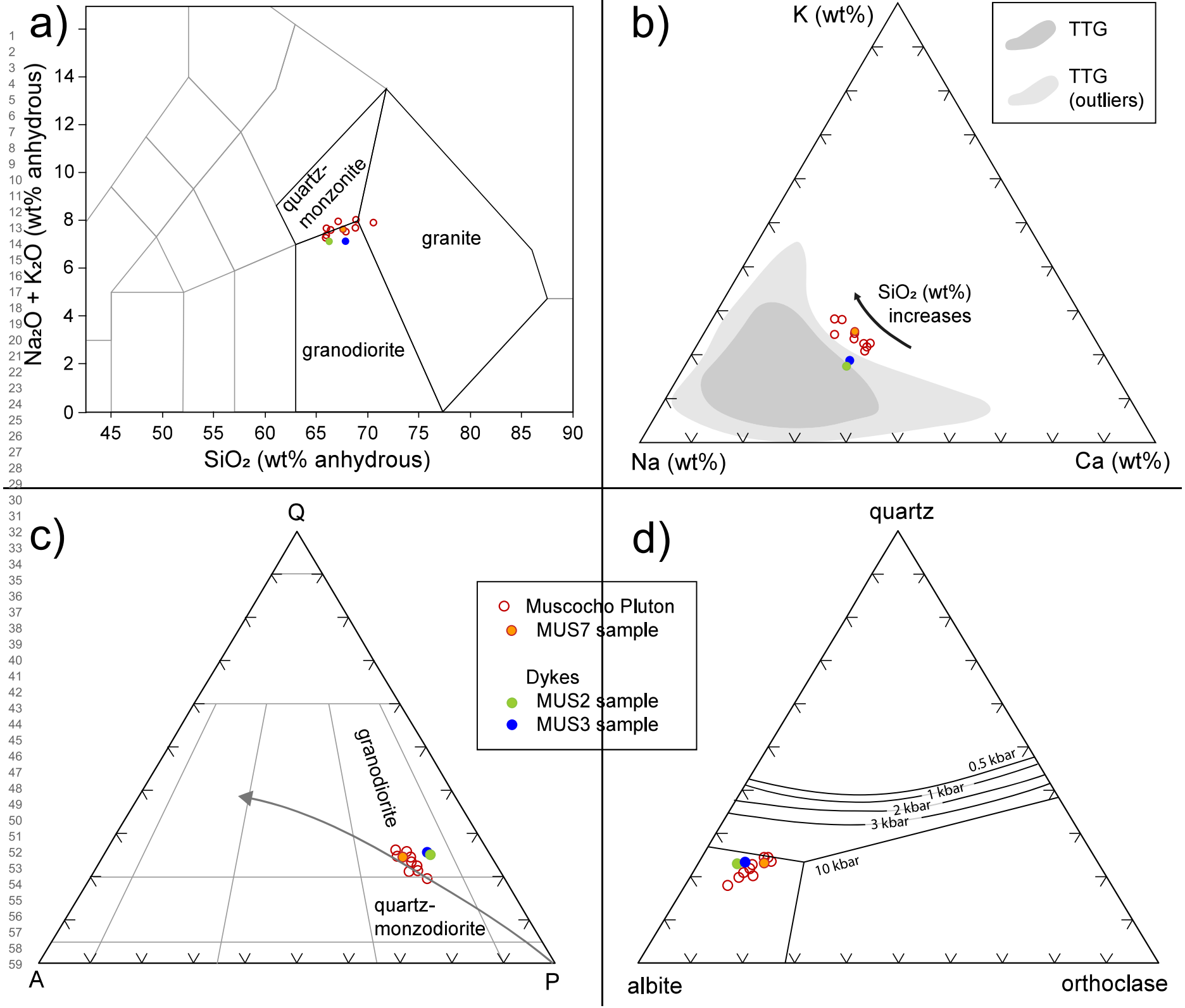
a)
Na₂O + K₂O (wt% anhydrous)
SiO₂ (wt% anhydrous)
quartz-
monzonite
granite
granodiorite
b)
K (wt%)
Na (wt%)
Ca (wt%)
TTG
TTG
(outliers)
SiO₂ (wt%)
increases
c)
Q
A
P
granodiorite
quartz-
monzodiorite
Muscocho Pluton
MUS7 sample
Dykes
MUS2 sample
MUS3 sample
d)
quartz
albite
orthoclase
0.5 kbar
1 kbar
2 kbar
3 kbar
10 kbar

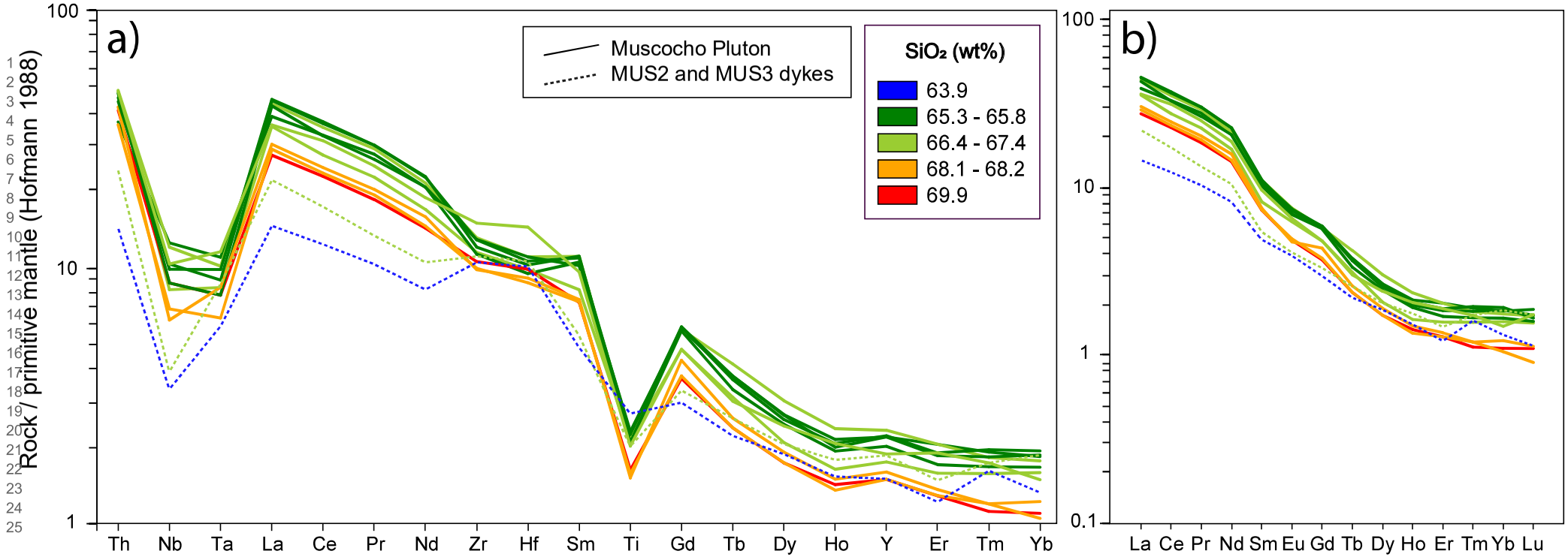
a)
b)
Muscocho Pluton
MUS2 and MUS3 dykes
SiO₂ (wt%)
63.9
65.3 - 65.8
66.4 - 67.4
68.1 - 68.2
69.9
Rock / primitive mantle (Hofmann 1988)
100
10
1
0.1
Th Nb Ta La Ce Pr Nd Zr Hf Sm Ti Gd Tb Dy Ho Y Er Tm Yb
La Ce Pr Nd Sm Eu Gd Tb Dy Ho Er Tm Yb Lu

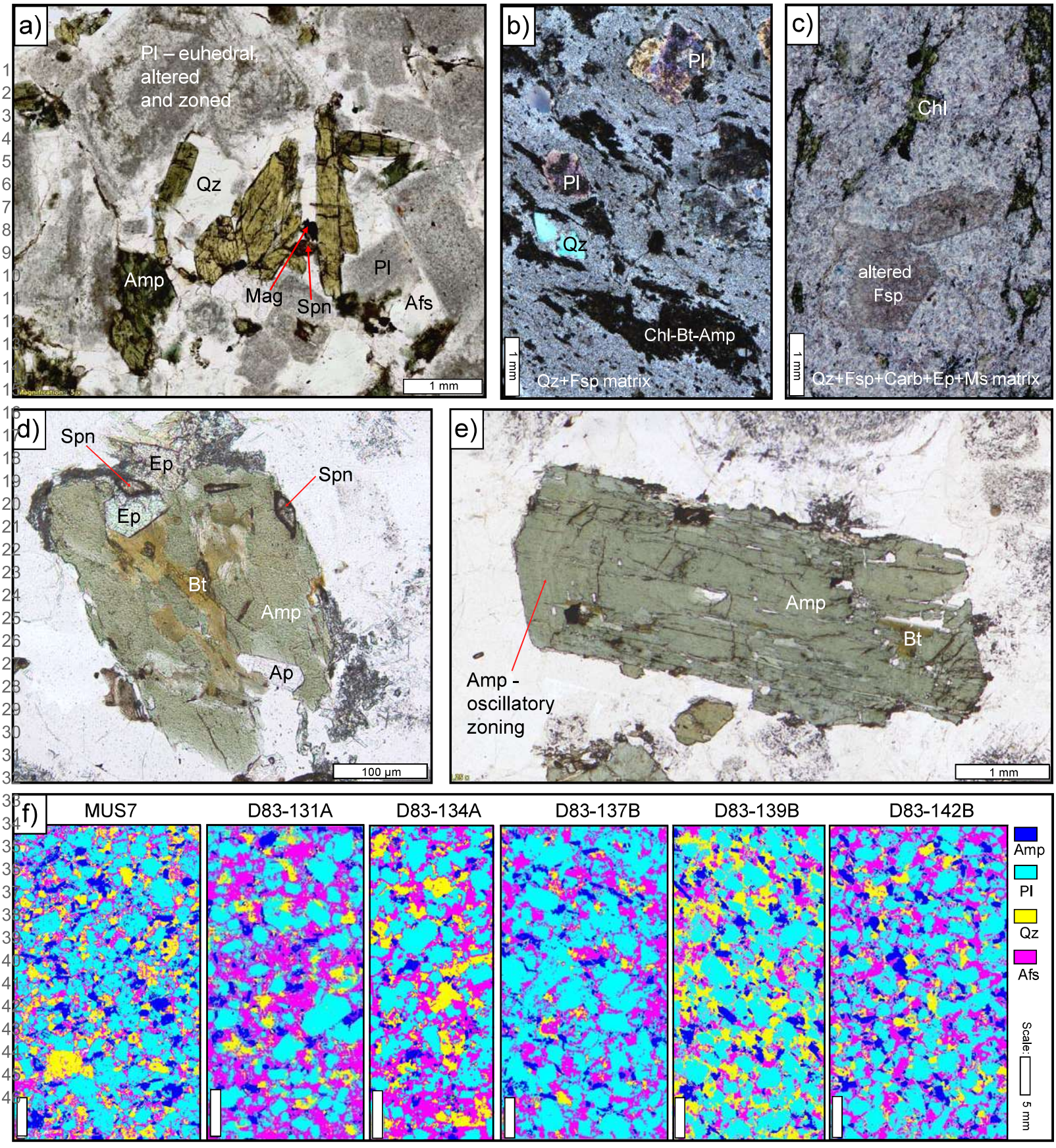
a)
Pl – euhedral, altered and zoned
Qz
Amp
Mag
Spn
Pl
Afs
1 mm
b)
Pl
Pl
Qz
Chl-Bt-Amp
1 mm
Qz+Fsp matrix
c)
Chl
altered Fsp
1 mm
Qz+Fsp+Carb+Ep+Ms matrix
d)
Spn
Ep
Spn
Ep
Bt
Amp
Ap
100 µm
e)
Amp
Bt
Amp - oscillatory zoning
1 mm
f)
MUS7
D83-131A
D83-134A
D83-137B
D83-139B
D83-142B
Amp
Pl
Qz
Afs
Scale:
5 mm

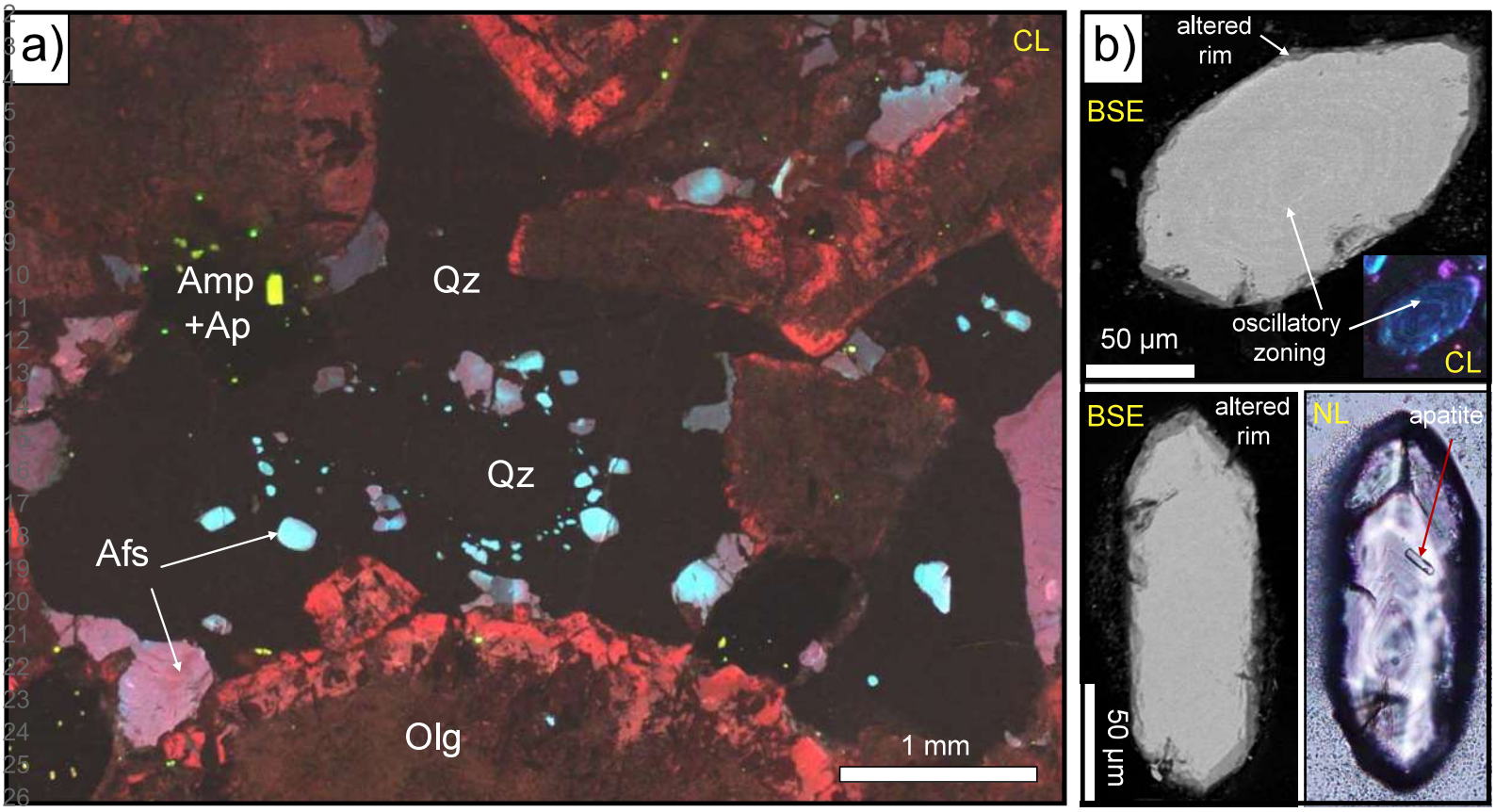
a)
CL
Amp
+Ap
Qz
Qz
Afs
Olg
1 mm
b)
altered
rim
BSE
50 µm
oscillatory
zoning
CL
BSE
altered
rim
50 µm
NL
apatite

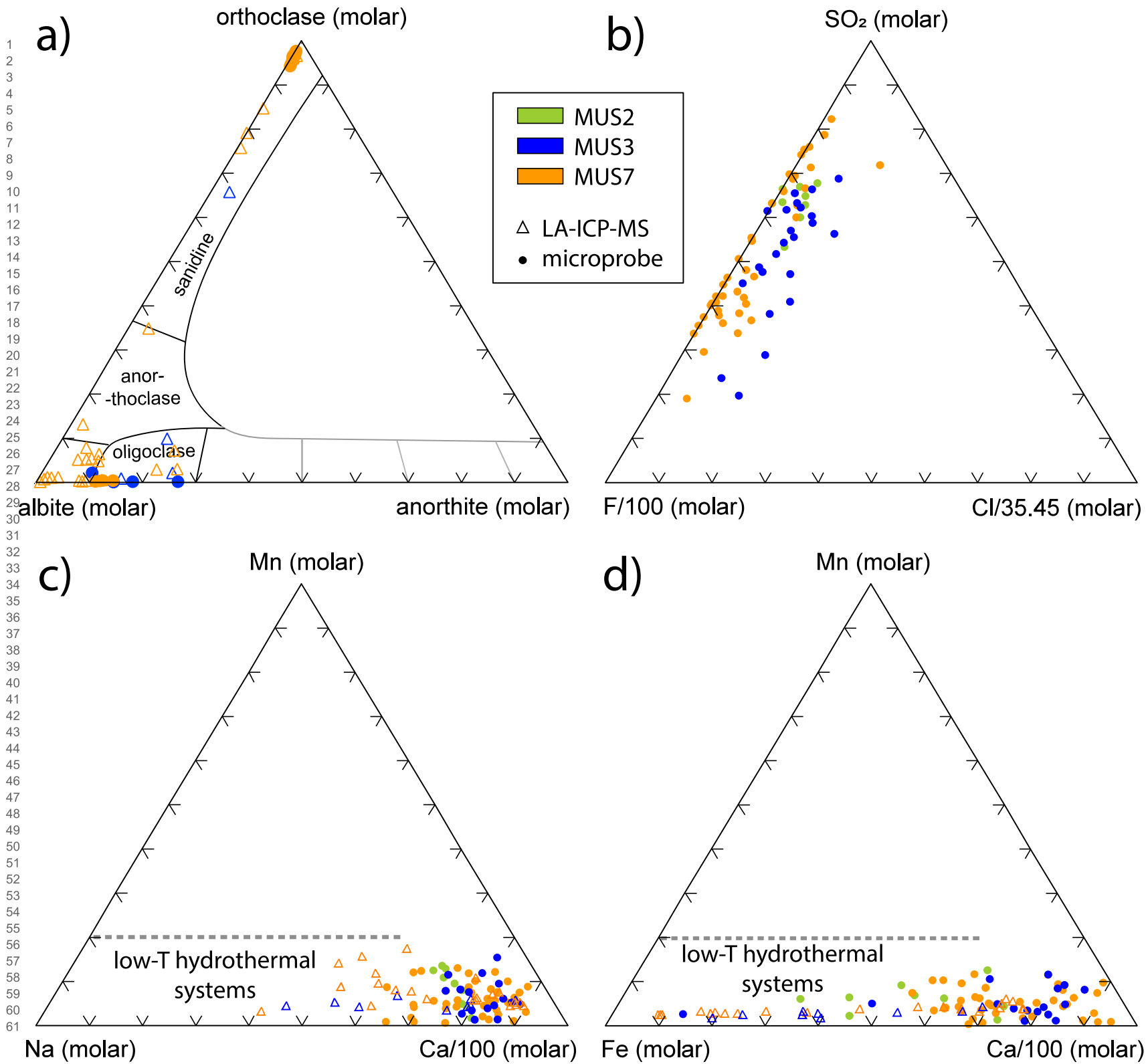
a)
orthoclase (molar)
sanidine
anor-
-thoclase
oligoclase
albite (molar)
anorthite (molar)
MUS2
MUS3
MUS7
LA-ICP-MS
microprobe
b)
SO₂ (molar)
F/100 (molar)
Cl/35.45 (molar)
c)
Mn (molar)
low-T hydrothermal
systems
Na (molar)
Ca/100 (molar)
d)
Mn (molar)
low-T hydrothermal
systems
Fe (molar)
Ca/100 (molar)

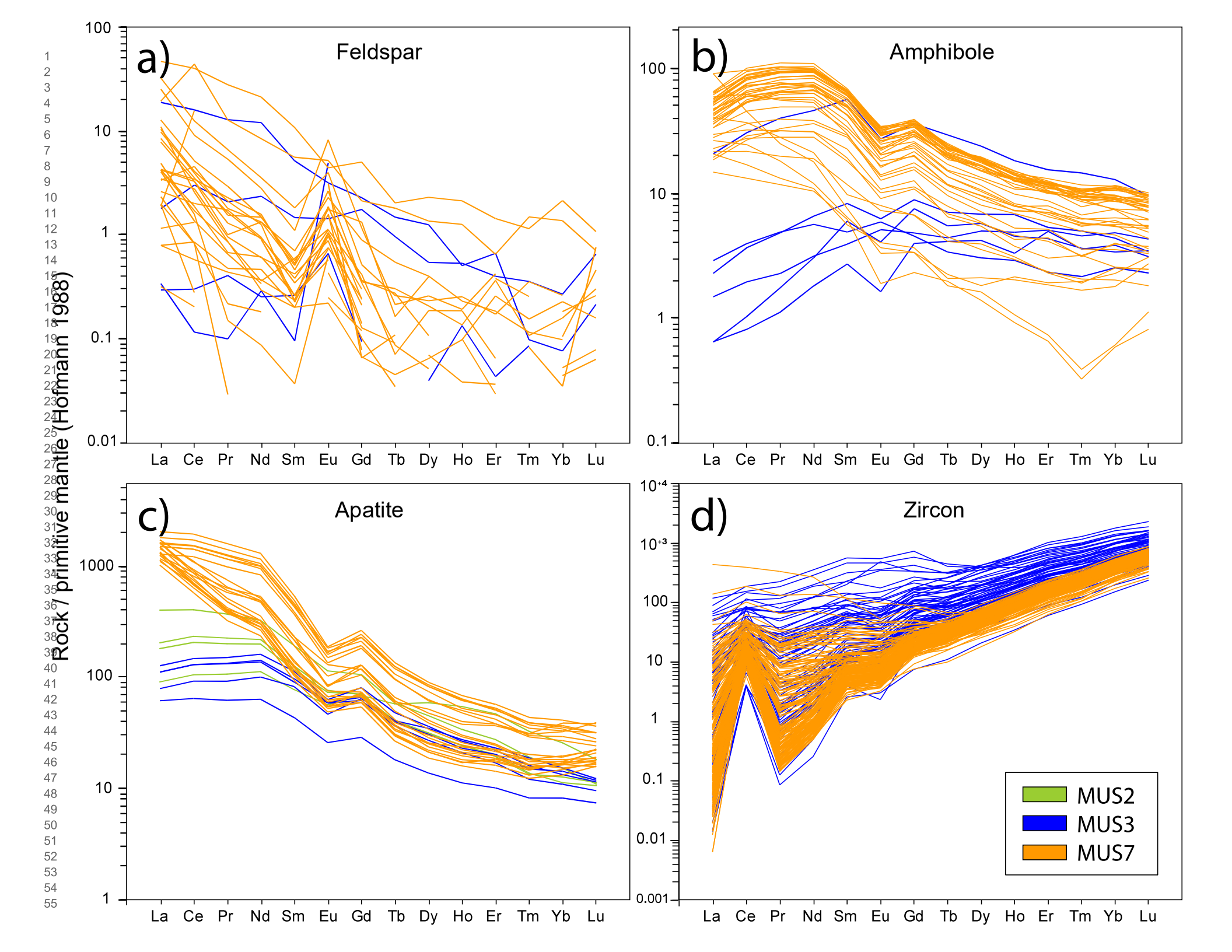
a)
Feldspar
b)
Amphibole
c)
Apatite
d)
Zircon
Rock / primitive mantle (Hofmann 1988)
La Ce Pr Nd Sm Eu Gd Tb Dy Ho Er Tm Yb Lu
MUS2
MUS3
MUS7

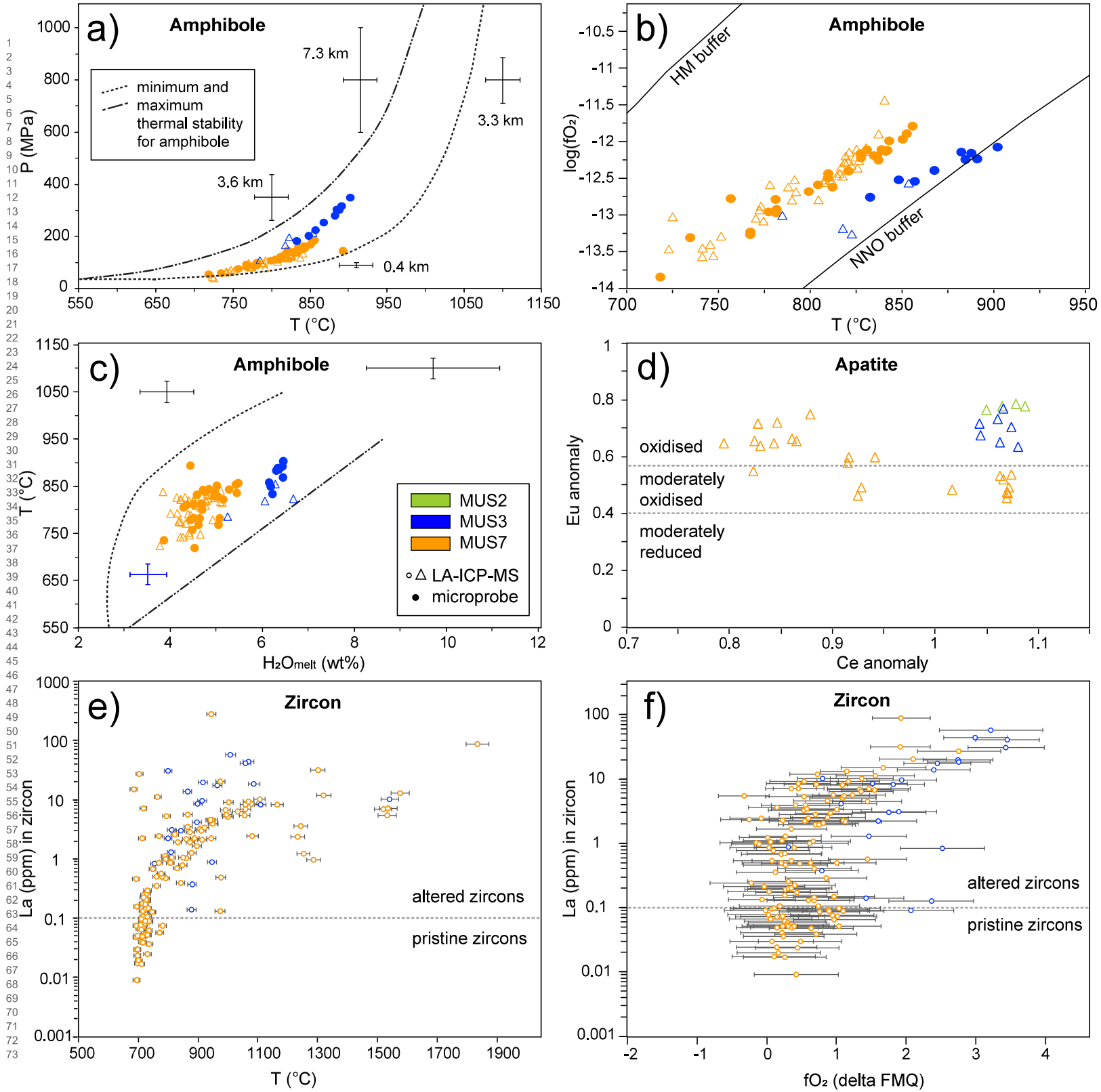
a)
Amphibole
minimum and
maximum
thermal stability
for amphibole
7.3 km
3.3 km
3.6 km
0.4 km
P (MPa)
T (°C)
b)
Amphibole
HM buffer
NNO buffer
log(fO₂)
T (°C)
c)
Amphibole
MUS2
MUS3
MUS7
LA-ICP-MS
microprobe
T (°C)
H₂Omelt (wt%)
d)
Apatite
oxidised
moderately
oxidised
moderately
reduced
Eu anomaly
Ce anomaly
e)
Zircon
altered zircons
pristine zircons
La (ppm) in zircon
T (°C)
f)
Zircon
altered zircons
pristine zircons
La (ppm) in zircon
fO₂ (delta FMQ)

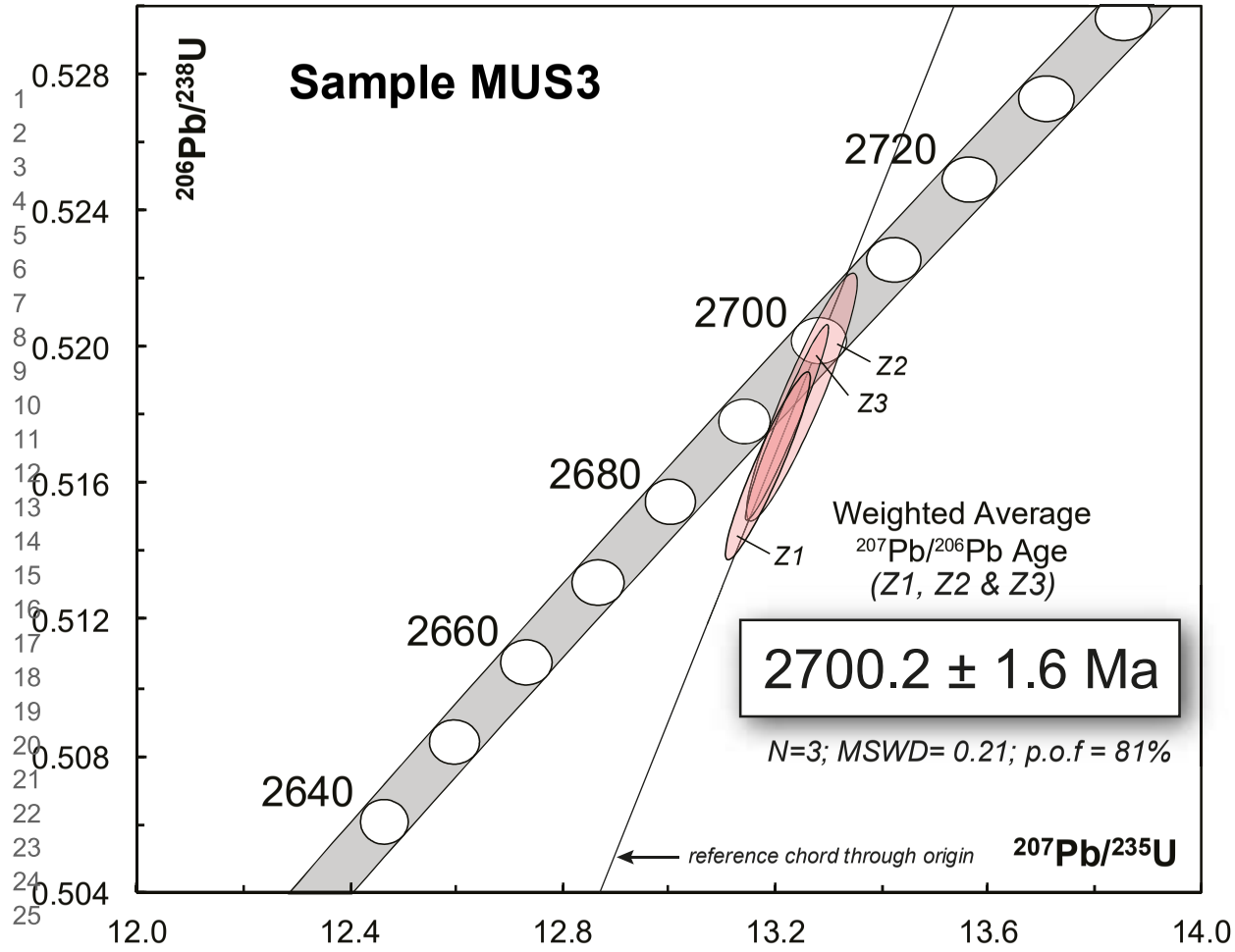
Sample MUS3
$^{206}Pb/^{238}U$
0.528
0.524
0.520
0.516
0.512
0.508
0.504
12.0
12.4
12.8
13.2
13.6
14.0
$^{207}Pb/^{235}U$
2720
2700
2680
2660
2640
Z1
Z2
Z3
Weighted Average
$^{207}Pb/^{206}Pb$ Age
(Z1, Z2 & Z3)
2700.2 ± 1.6 Ma
N=3; MSWD= 0.21; p.o.f = 81%
reference chord through origin

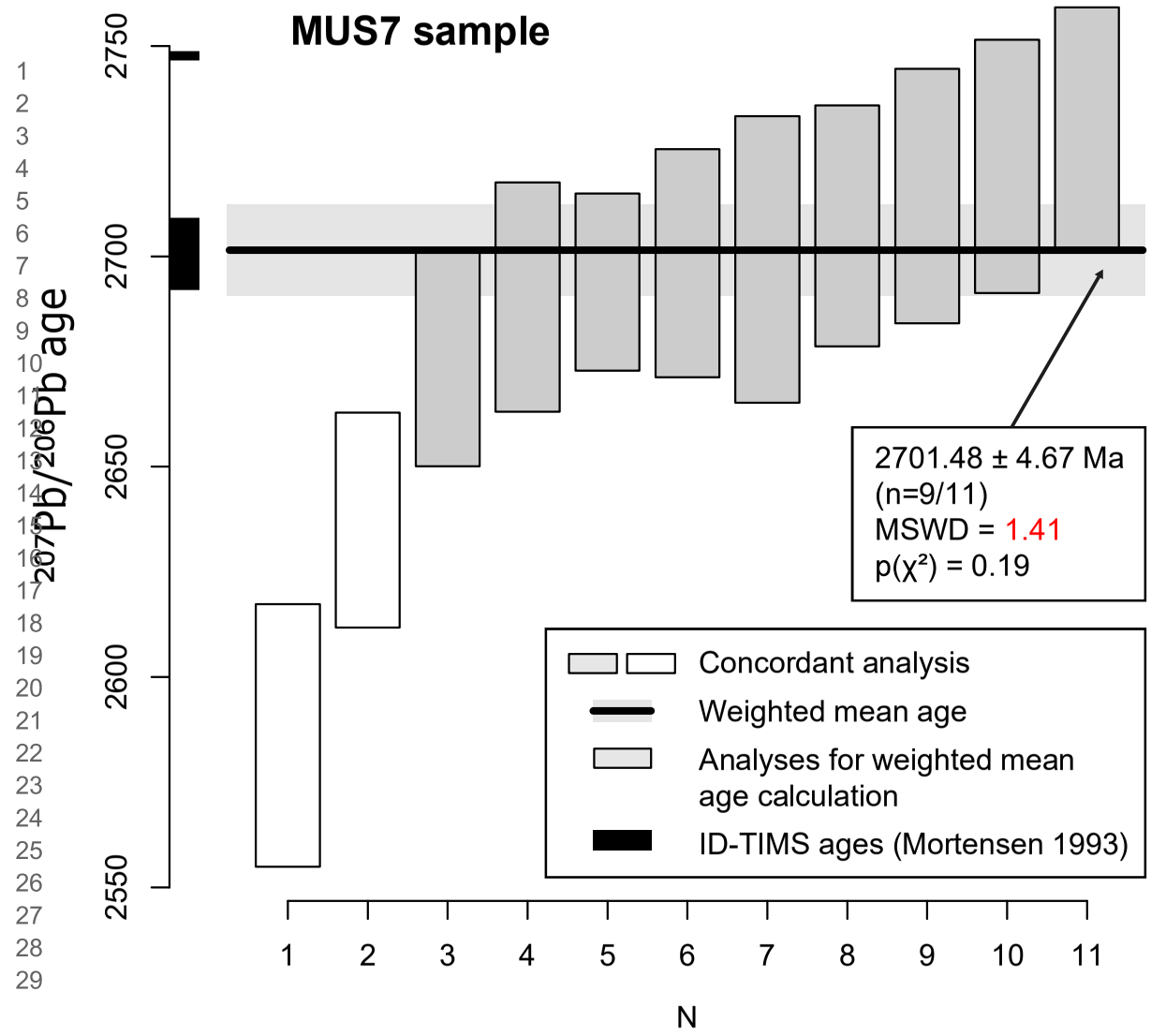
MUS7 sample
$^{207}Pb/^{206}Pb$ age
2550
2600
2650
2700
2750
1
2
3
4
5
6
7
8
9
10
11
N
2701.48 ± 4.67 Ma
(n=9/11)
MSWD = 1.41
p(χ²) = 0.19
Concordant analysis
Weighted mean age
Analyses for weighted mean age calculation
ID-TIMS ages (Mortensen 1993)

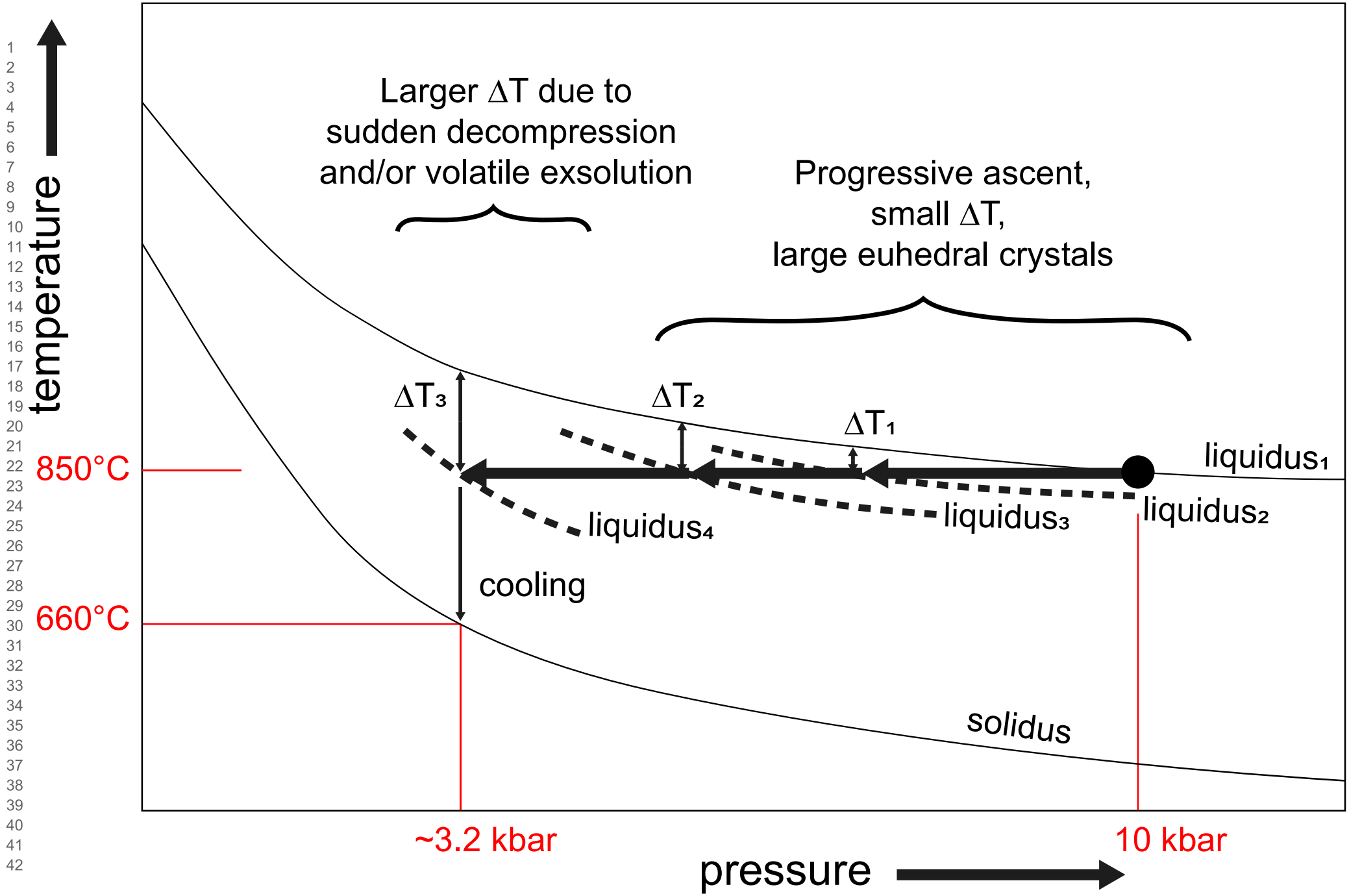
temperature
Larger ΔT due to
sudden decompression
and/or volatile exsolution
Progressive ascent,
small ΔT,
large euhedral crystals
ΔT3
ΔT2
ΔT1
liquidus1
liquidus2
liquidus3
liquidus4
cooling
850°C
660°C
solidus
~3.2 kbar
10 kbar
pressure

**Table 1:** Summary of physico-chemical parameters for the Muscocho pluton

| Parameter | MUS3 | MUS7 | Data |
|---|---|---|---|
| $a_{TiO_2}$ (1)* | 0.64 | 0.58 | whole-rock analyses |
| $fO_2$ (2) | / | moderately oxidized | $Fe_2O_3/Fe_2O_3T$ (whole rock) |
| $fO_2$ (3) | NNO ± 0.5 | NNO+1 ± 0.5 | amphibole (microprobe) |
| $fO_2$ (4) | NNO 0 to +1 | | Mn-in-apatite (LA-ICP-MS) |
| $fO_2$ (5) | oxidized | moderately oxidized | Eu anomaly, apatite (LA-ICP-MS) |
| $fO_2$ (6) | NNO+ 1.45 ± 1.14 | NNO -0.1 ± 1.17 | REE in zircon with La < 0.1 ppm (LA-ICP-MS) |
| $H_2O$ (7) | 6.32 ± 0.10 wt.% | 4.70 ± 0.38 wt.% | amphibole (microprobe) |
| P (8) | 2.79 ± 0.46 kbar | 1.39 ± 0.36 kbar | amphibole (microprobe) |
| P (9) | 4.47 ± 0.77 kbar | 2.90 ± 0.61 kbar | amphibole (microprobe) |
| T (10) | 1015 °C | 1030 °C | Zr-content (whole rock) |
| T (11) | 882 ± 19 °C | 821 ± 40 °C | amphibole (microprobe) |
| T (12) | 735 ± 40 °C | 710 ± 14 °C | Ti-in-zircon with La < 0.1 ppm (LA-ICP-MS) |
| T (13) | 632 ± 1.8 °C | 621 ± 17.5 °C | Ti-in-quartz (LA-ICP-MS) |

*The methods used are: 1) (Hayden and Watson, 2007); 2) (Middlemost, 1989); 3, 7, 8, 11) (Ridolfi et al., 2010); 4) (Miles et al., 2014); 5) (Azadbakht et al., 2018); 6, 12) (Smythe and Brenan, 2016); 9) (Mutch et al., 2016); 10) (Watson and Harrison, 1983); 13) (Wark and Watson, 2006).